2001-06

A hot-stage Atomic Force Microscope for the measurement of plastic deformation in metallic thin films during thermal cycling.

Shultz, Thomas E.

NAVAL POSTGRADUATE SCHOOL
Monterey, California

THESIS

A HOT-STAGE ATOMIC FORCE MICROSCOPE FOR THE MEASUREMENT OF PLASTIC DEFORMATION IN METALLIC THIN FILMS DURING THERMAL CYCLING

by

Thomas E. Shultz

June 2001

Thesis Advisor: Indranath Dutta

Approved for public release; distribution is unlimited

REPORT DOCUMENTATION PAGE			Form Approved OMB No. 0704-0188
Public reporting burden for this collection of information is estimated to average 1 hour per response, including the time for reviewing instruction, searching existing data sources, gathering and maintaining the data needed, and completing and reviewing the collection of information. Send comments regarding this burden estimate or any other aspect of this collection of information, including suggestions for reducing this burden, to Washington headquarters Services, Directorate for Information Operations and Reports, 1215 Jefferson Davis Highway, Suite 1204, Arlington, VA 22202-4302, and to the Office of Management and Budget, Paperwork Reduction Project (0704-0188) Washington DC 20503.			
1. AGENCY USE ONLY *(Leave blank)*	**2. REPORT DATE** June 2001	**3. REPORT TYPE AND DATES COVERED** Master's Thesis	
4. TITLE AND SUBTITLE: Title (Mix case letters) A Hot-Stage Atomic Force Microscope for the Measurement of Plastic Deformation in Metallic Thin Films during Thermal Cycling			**5. FUNDING NUMBERS**
6. AUTHOR(S) Thomas E. Shultz			
7. PERFORMING ORGANIZATION NAME(S) AND ADDRESS(ES) Naval Postgraduate School Monterey, CA 93943-5000			**8. PERFORMING ORGANIZATION REPORT NUMBER**
9. SPONSORING / MONITORING AGENCY NAME(S) AND ADDRESS(ES) N/A			**10. SPONSORING / MONITORING AGENCY REPORT NUMBER**
11. SUPPLEMENTARY NOTES The views expressed in this thesis are those of the author and do not reflect the official policy or position of the Department of Defense or the U.S. Government.			
12a. DISTRIBUTION / AVAILABILITY STATEMENT Approved for public release; distribution is unlimited			**12b. DISTRIBUTION CODE**

13. ABSTRACT ***(maximum 200 words)***

An Atomic Force Microscope is equipped with a hot-stage and a vacuum system in order to enable *in-situ* studies of plastic deformation and interfacial sliding of thin metallic films on Si substrates during thermal cycling. The apparatus can reach sample temperatures of 100°C while maintaining optimum resolution. The system will allow future *in-situ* thermal cycling experiments on microelectronic devices in a protected environment to provide insight into the role of plastic deformation in metallic thin films on the stability of future generations of device structures. The details of the design, along with the performance limitations of the system are discussed. Preliminary results demonstrating the performance of the system at an elevated temperature are presented. Limited *post-situ* results from direct measurement of the plastic deformation of thin Cu films on Si substrates induced by thermal cycling are also presented, primarily with the objective of establishing the need for detailed *in-situ* studies. While artifacts such as permanent dimensional changes of the film are observed *post-situ*, a detailed mechanistic understanding of the interaction between the temperature-dependent stress state of the film and the resultant inelastic deformation within the film and at the interface can only be obtained through *in-situ* experiments.

14. SUBJECT TERMS Atomic Force Microscopy, Creep Mechanisms, Hot-Stage, Interfacial Sliding, Microelectronic Devices, Thin Films, Vacuum System			**15. NUMBER OF PAGES** 120
			16. PRICE CODE
17. SECURITY CLASSIFICATION OF REPORT Unclassified	**18. SECURITY CLASSIFICATION OF THIS PAGE** Unclassified	**19. SECURITY CLASSIFICATION OF ABSTRACT** Unclassified	**20. LIMITATION OF ABSTRACT** UL

NSN 7540-01-280-5500

Standard Form 298 (Rev. 2-89)
Prescribed by ANSI Std. 239-18

THIS PAGE INTENTIONALLY LEFT BLANK

Approved for public release; distribution is unlimited

A HOT-STAGE ATOMIC FORCE MICROSCOPE FOR THE MEASUREMENT OF PLASTIC DEFORMATION IN METALLIC THIN FILMS DURING THERMAL CYCLING

Thomas E. Shultz
Lieutenant, United States Navy
B.A., Occidental College, 1994

Submitted in partial fulfillment of the
requirements for the degree of

MASTER OF SCIENCE IN MECHANICAL ENGINEERING

from the

NAVAL POSTGRADUATE SCHOOL
June 2001

Author: _____
Thomas E. Shultz

Approved by: _____
Indranath Dutta, Thesis Advisor

_____
Terry R. McNelley, Chairman
Department of Mechanical Engineering

THIS PAGE INTENTIONALLY LEFT BLANK

ABSTRACT

An Atomic Force Microscope is equipped with a hot-stage and a vacuum system in order to enable *in-situ* studies of plastic deformation and interfacial sliding of thin metallic films on Si substrates during thermal cycling. The apparatus can reach sample temperatures of 100°C while maintaining optimum resolution. The system will allow future *in-situ* thermal cycling experiments on microelectronic devices in a protected environment to provide insight into the role of plastic deformation in metallic thin films on the stability of future generations of device structures. The details of the design, along with the performance limitations of the system are discussed. Preliminary results demonstrating the performance of the system at an elevated temperature are presented. Limited *post-situ* results from direct measurement of the plastic deformation of thin Cu films on Si substrates induced by thermal cycling are also presented, primarily with the objective of establishing the need for detailed *in-situ* studies. While artifacts such as permanent dimensional changes of the film are observed *post-situ*, a detailed mechanistic understanding of the interaction between the temperature-dependent stress state of the film and the resultant inelastic deformation within the film and at the interface can only be obtained through *in-situ* experiments.

THIS PAGE INTENTIONALLY LEFT BLANK

TABLE OF CONTENTS

ACKNOWLEDGEMENTS

The author gratefully acknowledges the financial support of this research by the National Science Foundation under Contract # DMR-0075281, with Dr. Bruce A. MacDonald as the program monitor.

I would like to express my sincere gratitude and appreciation to Professor Indranath Dutta for his advice, support, patience, and motivation throughout the thesis process. I am also indebted to Mardo Blanco, Tom Christian, Frank Frandsen, Dr. Ashok Gopinath, Jim Lefler, Tom McCord, Dr. Terry McNelley, LT Keith Peterson and Don Snyder for their support and assistance.

Most of all I would like to thank my wife, Teri, and our daughter, Natalie. You have both given so much love and support while I was absorbed in graduate study. Your endless happiness and cheer gave me the strength to always push ahead.

THIS PAGE INTENTIONALLY LEFT BLANK

I. INTRODUCTION

Understanding the relationships between a material's chemical, physical, and mechanical properties is a key in determining its service application and performance. For example, the materials used to fabricate microelectronic devices must successfully perform their electronic functions, but they must also maintain reliability. Thus, they require a certain structural integrity and must provide adequate resistance to corrosive and mechanical failures that may arise in operation.

Many of the materials and devices that have led to the information revolution are in the form of thin films deposited on rigid substrates. These metal films or lines are mechanically constrained by the silicon substrate and encapsulating layers of silica or other dielectric materials. Ranging in size from a few nanometers to a few micrometers, thin films generally have properties different from their bulk counterparts, and their thermo-mechanical response may be influenced significantly by the underlying substrate [Refs. 1-4].

Typically, microelectronic devices are made by growing or depositing the various thin films onto a silicon substrate. Many of these processes occur at elevated temperatures and, due to differences in the coefficient of thermal expansion (CTE) between thin metallic films and semiconductor substrates, very large thermal stresses are induced during fabrication and can remain during its subsequent application. Although not as significant, changes in service temperatures also induce thermal stresses.

Previous studies have noted that due to these thermal mismatches, several plastic deformation mechanisms such as dislocation glide, dislocation creep and diffusional flow

may appear [Refs. 4-8]. In addition, since significant interfacial shear stresses exist near the edges of the film, permanent deformation of the film may also occur by diffusionally-controlled interfacial sliding resulting in a size change between the film and substrate [Refs. 9-13]. Possible failures such as open circuits from metal cracking and voiding, short circuits due to hillocks, and both open and short failures due to electromigration are all possible consequences leading to a decrease in the reliability of the microelectronic device [Refs. 1,8, 14-20].

Due to these consequences, a significant amount of research has centered on the effects of thermal cycling on thin films. The stress in thin films has been measured by a variety of methods, such as optical interferometry [Ref. 21], X-ray diffraction to measure the lattice spacing [Refs. 22-23] or to measure substrate curvature [Refs. 24-25], and laser scanning to measure substrate curvature [Refs. 1, 5, 7- 8, 14,18, 26-28]. In addition, numerous analytical and finite element models have been developed to model stress development and history in thin films [Refs. 4-6,16,29]. However, due to the nature of thin films, there are few methodologies for the measurement or modeling of the plastic deformation of thin films due to thermal cycling, with only *post-situ* analysis completed to date through the use of Atomic Force Microscopy [Refs. 9-10,30].

Since the current trend in microelectronics is towards more compact devices, a greater understanding of the effects of thermal cycling on thin films is in order. In addition, the continually shrinking submicron technologies have led to an increasing interest in alternatives to the predominant thin metal film: aluminum-based alloys. For instance, due to the fact that it is a significantly better conductor than aluminum, and that

its higher melting point should result in improved electromigration resistance, copper has increasingly been seen as a replacement of aluminum in thin metal films.

In addition to the development and use of various materials for thin metal films, there is also a large effort to substitute dielectric films with extremely low conductivities for the oxide films used in the past, especially for systems using thin copper films. However, these low conductivity dielectrics also possess a low stiffness, and hence provide less resistance to plastic deformation of thin metallic films.

In order to better understand the consequences of these microelectronic device fabrication developments, it is essential to be able to map the deformation history of thin metallic films subjected to thermal cycling. Therefore, this thesis incorporates a hot-stage and vacuum system into a commercial atomic force microscope (AFM) in order to enable future *in-situ* studies of plastic deformation and interfacial sliding of thin metallic films on Si substrates during thermal cycling. Limited *post-situ* results from direct measurement of the plastic deformation of thin Cu films on Si substrates induced by thermal cycling are also presented, primarily with the objective of establishing the need for detailed *in-situ* studies. While permanent dimensional changes of the film can be observed *post-situ* by Atomic Force Microscopy, a detailed mechanistic understanding of the interaction between the temperature-dependent stress state of the film and the resultant inelastic deformation within the film and at the interface can only be obtained through *in-situ* experiments.

THIS PAGE INTENTIONALLY LEFT BLANK

II. BACKGROUND

A. THERMAL EXCURSION OF MICROELECTRONIC DEVICES

In the early 1960s, constructing more than one transistor on a semiconductor substrate was considered cutting edge. Today standard microelectronic devices contain tens of millions of transistors. A general understanding of the different processes involved in microelectronic fabrication is key to any study of thin films and their response to thermally induced thermal stresses.

Figure 1 illustrates the basic sequence of events that can occur in the fabrication of a microelectronic device, in this case a simple diode [Refs. 19-20, 31]. The building block is the semiconductor substrate. The technique used to produce most of the crystals from which semiconductor wafers are cut is called *Czochralski growth* or the "CZ" method. Single-crystal silicon *boules* up to 300mm in diameter and 1 to 2 meters long are generally formed. The key to the process is controlling impurities and limiting the number of crystal defects. Impurities termed dopants are often intentionally added during crystal growth to manipulate the charge carrier density of the crystal, making it either "n-type"(electron-rich) or "p-type"(electron-poor). The *boule* is checked for defects and then sliced into round wafers and packaged for processing.

Basic processing and pattern transfer occur next. Direct oxidation or Chemical Vapor Deposition (CVD) are the general processes in which protective and/or insulative layers and films of materials such as Silicon Dioxide (SiO_2), Silicon Nitride (Si_3N_4), or dielectric materials can be applied. Next, optical lithography and etching are used for pattern creation in which a photomask of the layout is transferred to the substrate by

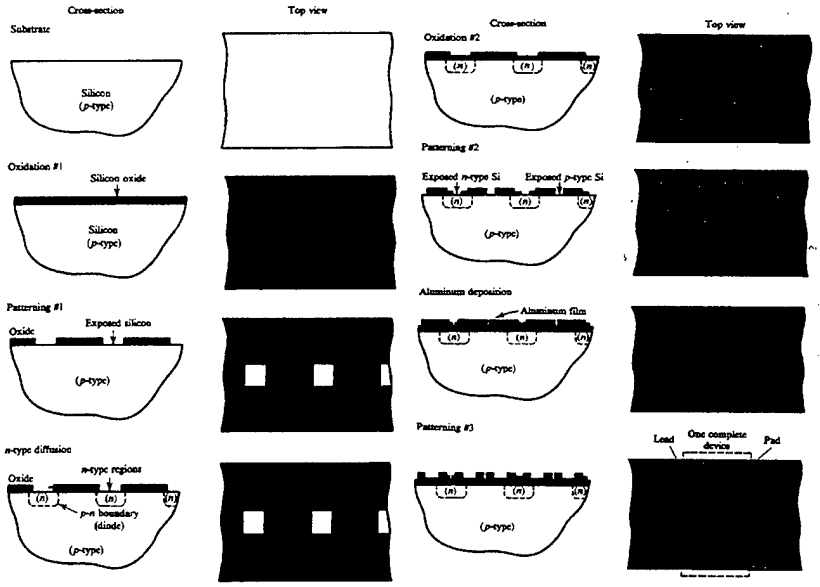

Figure 1: Basic steps in microelectronic fabrication [From Ref.20]

radiating a photoresist. The pattern is etched away and is now ready for the diffusion of additional dopants. By oxidizing the substrate, etching a pattern of holes into the oxide, and diffusing impurities through the holes, the semiconductor substrate is now an electrical device. Though functional, these devices must now be connected with each other and the outside world to form a useful circuit. This is done through the application of thin metallic films. Vacuum deposition techniques such as evaporation and sputtering are generally used for metallic thin film application. Dielectric materials such as polyimide are often applied to physically separate the current carrying conductive thin films. These processes can then be repeated in various intervals until the desired multi-layer microelectronic device is completed. The device is then packaged to provide mechanical support, electrical connection, protection, and heat removal, and is now ready for service.

One of the key factors in each of these steps is the temperature of the wafer or substrate during processing. These processes generally take place at elevated temperatures. For example, in chemical vapor deposition, the wafer temperature may be anywhere between 250 to 450°C during deposition while the application of the photoresist is generally proceeded by a dehydration bake of up to 250°C [Refs. 19-20, 31]. In addition, thin metallic film deposition also takes place at elevated temperatures up to 450°C [Ref. 19]. In device technology at or below the 0.13 micron technology node, electroplated copper thin film lines embedded in trenches within an inter-layer dielectric (ILD) are exposed to a cure temperature of ~450°C. Since multiple layers of these Cu-low K dielectric structures are deposited on the device, the structure is subjected to several thermal cycles, each corresponding to the fabrication of one layer. A combination of these temperature variations during different processing steps and/or service use can lead to severe stresses and strains in the film stack and the interfaces arising due to the thermal expansion mismatch between the metallic films, the silicon substrate, and the various dielectric layers.

B. METALLIC THIN FILM FAILURES

One of the most serious issues in the design and fabrication of microelectronic devices is ensuring the reliability of the metal interconnects. These metallic thin films provide electrical connections to the millions of electronic devices on a chip. As mentioned, since the substrate and metallic thin films used have different coefficients of thermal expansion, the resulting stresses and strains that arise during thermal variations

may result in device failure. Understanding the different failures possible is also key in any design or study of microelectronic devices.

Consequences of inhomogeneous plastic deformation that can occur in microelectronic devices are passivation cracking, hillock formation, and interfacial fracture or sliding. In passivation cracking, dislocation pileups can accumulate and slip causing cracks in the passivation film (Figure 2) [Ref. 1]. One of the purposes of the passivation glass is to constrain the underlying metal layer from deforming by diffusional processes. A crack in the passivation removes the constraint at that location and can allow a net flux of interconnect material to flow to that area, leaving a material deficiency elsewhere in the interconnect line. In hillock formation, grain boundary sliding can form spikes or hillocks projecting upward from the surface (Figure 2) [Ref. 1]. Both these failures have two negative consequences. First, the point of material deficiency usually contains voids or cracks that can lead to degradation in corrosion resistance or even an open circuit. Second, the protrusion of the interconnect material through the crack in the passivation can cause shorts to develop between one metal layer and another. In interfacial fracture or sliding, induced thermal stresses again can lead to failure of the interface or dimensional changes between the metallic thin film and substrate, resulting in possible failure of the microelectronic device [Refs. 9-10]. Interfacial fracture or sliding may also lead to passivation cracking or hillock formation in order to relax the induced stresses from the dimensional change between the substrate and metallic thin film.

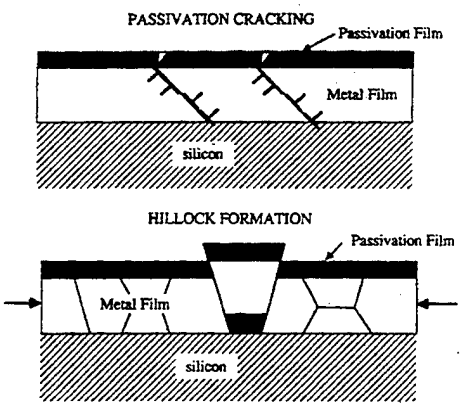

Figure 2: Mechanisms of inhomogeneous deformation in thin films [From Ref. 1]

There is also the push by industry to continually decrease the size of metal interconnects while increasing their current density. In addition to increased stresses that may be induced, this may also cause failure of the microelectronic device by the mechanism of electromigration (Figure 3) [Refs. 15,19-20]. In electromigration, metal moves in the direction of current, chiefly along grain boundaries. Voids are left as metal is removed from the "upstream" grains while mounds of extra metal or hillocks accumulate "downstream". As before, these voids can produce resistive heating, accelerating the process, and eventually leading to device failure.

It is therefore obvious that a detailed understanding of the effects of material selection, microstructure, fabrication techniques, and interfacial characteristics is crucial to the enhanced reliability of the microelectronic device.

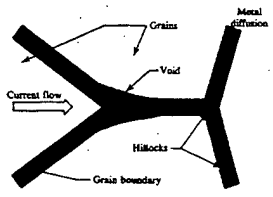

Figure 3: Mechanism of electromigration [From Ref. 20]

C. ATOMIC FORCE MICROSCOPY

1. Basic Operating Principles

Atomic Force Microscopy is just one of several technologies collectively known as Scanning Probe Microscopy (SPM) [Refs. 32-33]. The atomic force microscope (AFM), as first described by Binning et al. in 1986 [Ref. 44], has recently become a widely used technique for the study of surface topography and surface forces of a variety of materials such as solid crystals, polymers, biological systems, and molecular crystals, with nanometer scale resolution. In theory, all SPM technologies are based on the interaction between a submicroscopic probe and the surface of the sample material. The difference between various SPM technologies is the nature of the interaction. In Atomic Force Microscopy the probe makes physical, albeit gentle, contact with the sample.

Experiments were conducted using a Burleigh® VISTA-100 atomic force microscope (AFM) (Figure 4). As in other AFMs, the VISTA-100 AFM contains a tip that is integrated at the end of a cantilever (spring) and is brought within the interatomic separations of a surface. Forces act on the tip and cause the cantilever (spring) to deflect while a position detector monitors the cantilever position. The output of the detector is connected to a feedback controller which regulates the force between the sample and the tip by moving the tip up or down. Movement of the tip is controlled by a piezoelectric ceramic (PZT) actuator. Figure 5 shows the basic elements of an AFM.

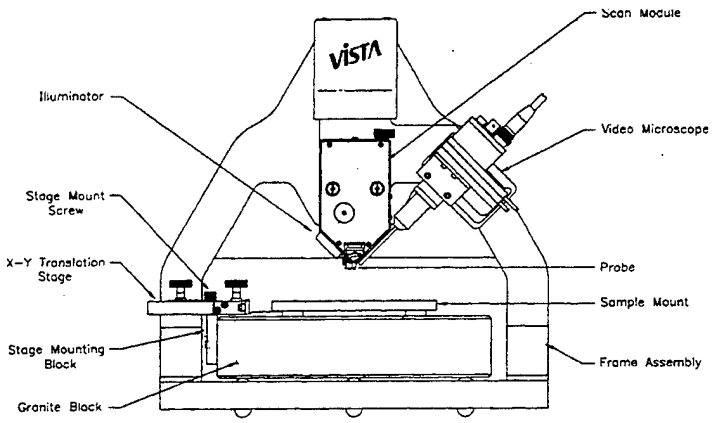

Figure 4: Vista-100 atomic force microscope (AFM) [From Ref. 32]

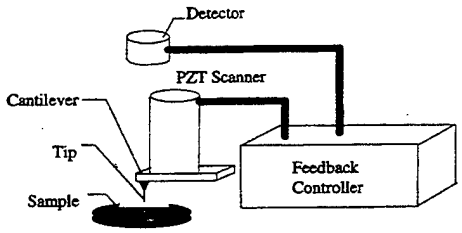

Figure 5: Basic elements of an AFM [From Ref. 32]

As the tip is rastered across the surface, it bounces up and down with the contours of the surface. By measuring the displacement of the tip (ie. the deflection of the cantilever), one can map out the surface topography with atomic resolution. This is achieved by designing a cantilever soft enough to deflect a measurable amount without damaging the surface features of the sample. The amount of deflection is proportional to the force acting on the tip:

$$F_{spring} = -k \bullet \Delta Z$$

where F is the force on the sample, k is the spring constant of the cantilever, and ΔZ is the deflection of the cantilever. Thus, for a "soft" cantilever, you need a spring constant weaker than the equivalent spring between atoms. For example, the vibration frequencies

ω of atoms in a crystalline solid are typically 10^{13} Hz or higher, while the mass of an atom is of the order of 10^{-25} kg. This means the interatomic spring constant, given by $\omega^2 m$, is of the order of 10 N/m.

2. Forces in Atomic Force Microscopy

An AFM measures the interaction forces between a tip and a sample surface. The sensing tip of the probe however consists of about 10^{15} atoms. The atoms at the very end of the tip interact with the surface through short-range forces, such as quantum mechanical repulsion forces, covalent bonding forces, and metallic adhesion. However, the long-range forces, such as Van der Waals forces, interact with a larger part of the tip. These long-range forces, called *many body interactions*, take a different form and are integrated over the entire body of the tip. In addition, since the tip and surface may be interacting through air, other gases, or liquids, the environment also plays an important role in interaction forces.

As stated, several factors contribute to the image contrast and care is required when interpreting atomic resolution images. Factors affecting the short-range forces include quantum mechanical exclusion forces, bond formation, adhesion, friction, and deformations. Quantum mechanical forces are repulsive forces that hinder the tip from penetrating the sample. Possible ionic, covalent, and metallic bond formation between tip and sample contributes to attractive forces. Adhesion is due to electron clouds overlapping. Frictional forces are orthogonal to the tip-sample contact force and tend to twist the cantilever while elastic and plastic deformation of the sample and tip are also due to strong short-range interactions.

Long-range forces, resulting from *many body interactions* of a large part of the tip with the sample surface, can extend to hundreds of angstroms. Factors affecting the long-range forces include Van der Waals forces, capillary forces, magnetic forces, and electrostatic forces. Van der Waals forces are attractive forces that can be approximated by assuming the tip is a sphere and integrating the forces between the sphere and surface. In ambient conditions, capillary forces also play an important role. In air, water vapor plays the dominant role with sample surfaces inherently covered with a layer of water contamination with a thickness of 50 ⊕ to 500 ⊕. Magnetic and electrostatic forces are also important, acting as attractive forces between tip and sample.

In general, attractive forces dominate the long-range interactions while the short-range forces are dominated by repulsive interaction. A generic interatomic force response curve is shown in Figure 6.

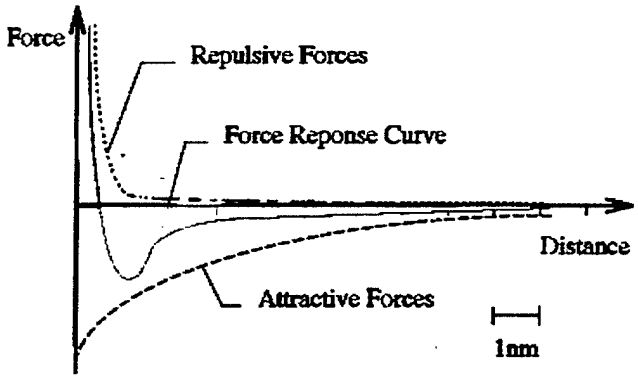

Figure 6: Generic interatomic force-distance curve

The ultimate resolution of the AFM is determined by the spatial dependence of the tip's interaction with the sample. If you operate an AFM with a tip/sample separation of a few nanometers, the long-range forces dominate. With increasing tip-sample distance, these attractive forces diminish at a much slower rate than the repulsive forces.

In the attractive force mode of operation, the image resolution is relatively poor because the image data is a convolution of the macroscopic shape of the tip. However, when the separation between the sample and the tip is reduced to less than a nanometer, the repulsive forces dominate. The repulsive forces are larger in magnitude than the attractive forces and localized to a much smaller portion of the tip. Thus, higher image resolution is possible at the expense of tip and/or sample damage.

3. Atomic Force Microscope Operation

a. Basic Functioniong

The essential components of the VISTA-100 AFM are shown in Figure 7. AFMs use the principle of negative feedback to control the tip-sample separation. A laser beam is bounced off a mirror and focused onto the end of the cantilever, opposite the tip while the back surface of the cantilever reflects the beam onto a split photo diode detector. The reflected beam is focused onto the middle of the split detector so that the difference signal is zero. When the cantilever deflects up or down in response to atomic force variations between sample and tip, the beam moves on the detector. The measured force is compared to a user selectable reference force to determine the error. The negative feedback loop moves the tip as needed to eliminate the measured error and maintain the desired interaction force. The tip is moved vertically (Z-direction) using a PZT scanning tube position actuator, with the PZT scanning tube also moving the tip in the X and Y direction for the rastering portion of the scan. The tip is raster scanned over the sample while the feedback adjusts the tip position for a constant force. The tip's position in the Z-axis direction, commanded by the feedback, corresponds to the

topography of the surface. To construct a 3-d image of the surface, the computer records these Z-axis movements as a function of the tip's X and Y position.

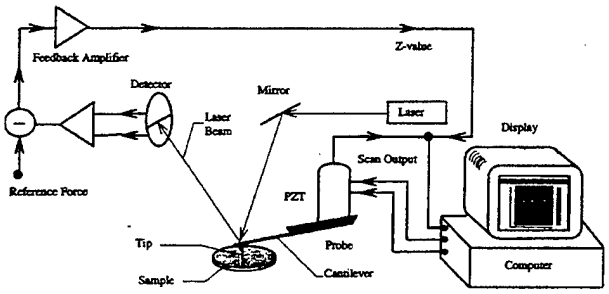

Figure 7: Essential components of the VISTA-100 AFM [From Ref. 32]

b. Piezoelectricity and PZT Scanning Tubes

As mentioned previously, motion of the tip within a few angstroms of the sample is accomplished using piezoelectric ceramics (PZT). An electric field applied across a piezoelectric ceramic causes expansion in one direction and contraction in another. The sensitivity of a piezoelectric ceramic depends on the particular arrangement of the atoms in the crystal and its thickness. The sensitivity of the piezoelectric materials used in the VISTA-100 AFM is about 2000 ⊕/volt, while the computer can control voltages with millivolt accuracy. Thus, the motion of the tip can be controlled with angstrom sensitivity.

Three-dimensional motion is achieved by shaping a PZT ceramic into a hollow cylinder. In the VISTA-100 AFM, a tip is attached to the bottom of the cylinder, while the top of the piezoelectric is fixed. Four electrodes are formed on the outside of the cylinder and one electrode is formed on the inside of the cylinder. By independently controlling the voltages applied across these electrodes, the piezoelectric cylinder can bend in any direction and be extended and retracted.

In Figure 8a, a negative voltage is applied to the four outside electrodes and a positive voltage is applied to the inside electrode. The electric field, therefore, points from the inside to the outside of the cylinder. This is opposite the poled direction of the tube. The cylinder will shrink between the electrodes (ie. the wall will become thinner) and, to keep the volume constant, the tube will become longer. If an opposite polarity is applied to the electrodes, the reverse will happen and the tube will shrink.

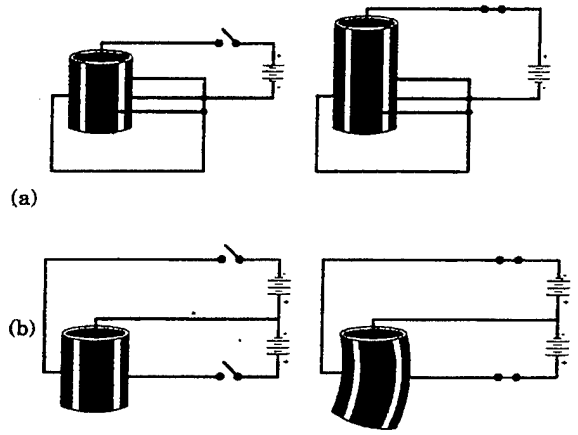

Figure 8: Cylindrical PZT with applied voltages for (a) vertical motion and (b) horizontal motion [From Ref. 32]

In Figure 8b, a positive voltage is applied to the left electrode, a negative voltage to the right electrode, and the other electrodes are held at ground. In this example, the left side of the tube will shrink and the right side of the tube will lengthen, with the front and back of the tube staying the same length. The tube can accommodate this shrinking and growing by bending to the left (X direction). If an opposite polarity is put on the left and right electrodes, the tube will bend to the right. For small amounts of bending, the fact that the tip also moves down as well as to the right and the left is neglected. If voltages are applied in the same way across the front and back electrodes,

the tip bends to the front and to the back (Y direction). The voltages to the left and right electrodes and to the front and back electrodes can be applied simultaneously to move the tip in any direction in the X-Y plane. A voltage applied to the inside electrode will cause the end of the tube to move up and down (Z direction) while still moving in X and Y. By applying voltages in this way, the end of the PZT scanning tube can be positioned anywhere within the 3-d region within angstrom resolution.

Inherent to PZT motion is some nonlinearity. For large voltages this becomes more obvious. In addition, the end of the PZT scanning tube moves in an arc and has some hysteresis. These motion errors are larger for higher voltages (motions) and are usually corrected by post linearization of the data using error correction software.

c. Vibration Isolation

Walking around a room causes desks and chairs to vibrate with an amplitude of about 1 μm or 10,000 ⊕. In order to hold the sample and tip only a few angstroms apart without having them crash into each other, the AFM is designed as a rigid body so it will vibrate as a whole and the sample-tip separation will not be affected. However, since this technique is never fully ideal, we have used a Kinetic Systems 9211 Series Labmate II Vibration Isolation Table as the system platform (Figure 9). This table performs automatic leveling, and vertical and horizontal vibration isolation through the use of an active-air suspension. Thus, through the use of the vibration isolation table and limiting the amount of acoustic noise, background effects are minimized, and the atomic resolution of the AFM is maintained.

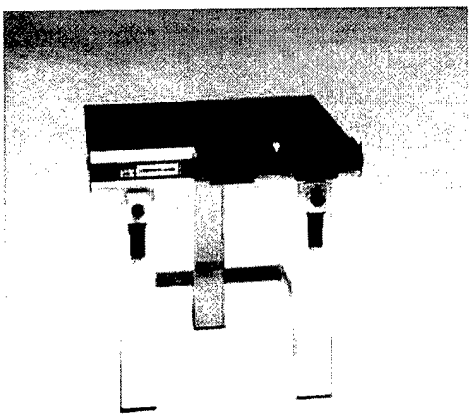

Figure 9: Kinetic Systems 9211 Series vibration isolation table

d. Modes of Operation

As stated previously, the interactions between sample and tip are classified by attractive long-range forces and repulsive short-range forces as characterized by the generic Force-Distance curve (Figure 6). When the tip approaches the sample, the cantilever remains undeflected until long-range forces influence the sample-tip junction. This means that the attractive forces initially become stronger until the repulsive forces become dominant forces. Initially, the cantilever is undeflected and there are no interaction forces (Figure 10a). As the separation between the sample and tip decreases, the capillary forces dominate and attract the tip so that the cantilever deflects downward (Figure 10b). This causes the cantilever to exert an upward force while the meniscus formed around the tip pulls the probe down through capillary forces. The result is a downward net force on the surface. Defining $F_{surface}$ as the reaction force, this force equals the sum of the cantilever force, $F_{cantilever}$, and the capillary forces, $F_{capillary}$, but it points in the opposite direction.

As the sample is driven closer to the probe, the cantilever bends back to its neutral state (Figure 10c). The cantilever force is zero and the force on the surface is equal to the capillary forces plus the attractive adhesion force between the tip and the surface. Continuing the motion and bringing the tip closer to the sample would deflect the cantilever upwards. At this point the repulsive forces are dominating the interaction, and they drive the tip away from the surface. The capillary and adhesion forces are still present. The interaction force on the sample is now completely switched in one direction and points upward (Figure 10d).

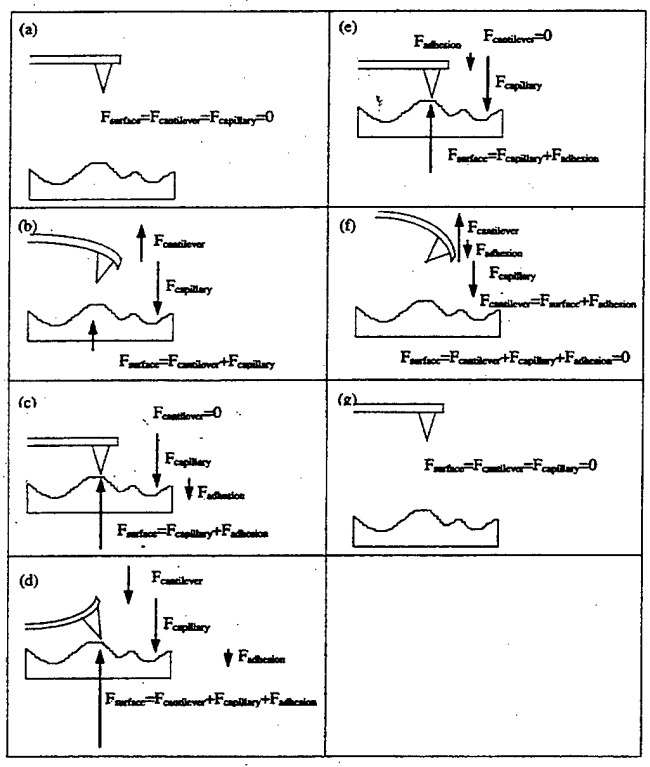

Figure 10: Interaction of tip and sample [From Ref. 32]

When the motion is reversed and the tip is retracted away from the sample, the cantilever goes through another neutral state (Figure 10e). But as the tip is retracted, the cantilever starts bending down (Figure 10f) (beyond the amount it deflected in Figure 10b). The cantilever bends downward until the cantilever spring force equals these attractive forces. At this point, the force on the surface is zero. Beyond this point the cantilever springs back up to its neutral position (Figure 10g). The motion of the tip as measured by the detector is shown in Figure 11 with each point corresponding to different steps in Figure 10. This shows the hysterisis in the force curve as the tip approaches then retracts from the surface.

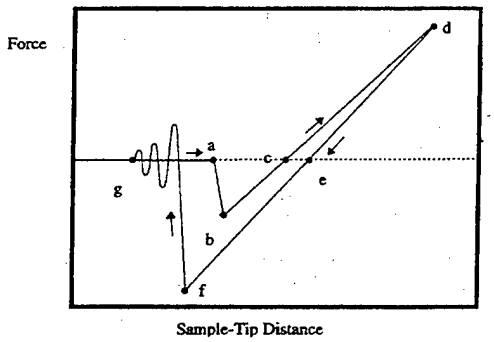

Figure 11: Typical AFM force curve [From Ref. 32]

There are two distinct types of interaction, attractive and repulsive, corresponding to two distinct modes of operation, non-contact (tapping) and contact. Proper contact mode operation requires that the sample and tip be engaged and operating around the point (c) where repulsive forces dominate. Hence, the sample and tip are in constant contact, albeit gentle. This point of operation is necessary because the attractive forces are dominated by capillary forces which vary from site to site on the sample and can vary the force and alter the amount the cantilever bends. The feedback responds to

these "faulty" height changes and interprets the force changes in topography of the sample. Additionally, attractive interactions are integrated over the macroscopic shape of the tip resulting in lower resolution than contact or repulsive mode.

The advantage of operation in the non-contact (tapping) or attractive mode, however, is operation at a further distance from the sample with much smaller force than in contact mode. This larger distance and lower force reduces the possibility of sample and/or tip damage. To image in this regime, a PZT engine is used to drive the cantilever at or near its resonant frequency. Changes in oscillation amplitude or phase correspond to changes in the force interactions between the sample and the probe.

D. INTERFACIAL SLIDING

1. Composite Systems

In a continuous fiber reinforced metal-matrix composite, due to the difference in the coefficients of thermal expansions of the matrix and the reinforcement, large internal stresses occur when the composite undergoes thermal cycling. In general, assuming a solid interfacial bond, continuous fiber reinforced composites are generally believed to deform in an isostrain condition, with the matrix and reinforcement experiencing the same strain history. However, there is evidence that even without interfacial fracture, dimensional changes and strain differences can occur between the matrix and reinforcement during thermal cycling [Ref. 13].

In one experiment by Funn and Dutta, model single fiber composite (SFC) systems with a lead matrix and either a quartz or nickel reinforcement were used to study the role of interfaces during isothermal creep at constant applied load [Ref. 13]. An

experimental apparatus was developed allowing the interface to be loaded in shear while also allowing for the heating of the SFC specimen.

Experimental data revealed that the fiber-top experienced a downward displacement (the shear direction) over time with respect to the matrix, with the amount of displacement increasing with both an increase in shear and temperature. Since there was no evidence of interfacial fracture, it was inferred that diffusionally accommodated interfacial sliding was responsible for the dimensional change. In addition, since neither the fiber nor the matrix were observed to creep measurably, the fiber-top displacement rate represented the average interfacial shear displacement rate ($\dot{\bar{U}}$) and was shown to be

$$\dot{\bar{U}} = K(\tau_{ave} - \tau_0)\exp[-Q_i / RT] \quad (Eq.1)$$

where K is a proportionality constant.

A constitutive law for diffusion-controlled interfacial sliding was then developed based on the continuum grain boundary sliding model of Raj and Ashby [Refs. 13, 35]. As in Raj and Ashby, the interface was considered to have a periodic topography (Figure 12a).

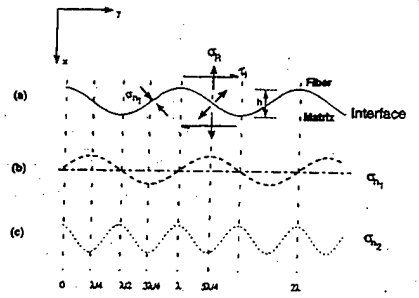

Figure 12: (a) Idealized representation of the periodicity of the fiber-matrix interface along the fiber length. (b) Distribution of normal stress (σ_{n_1}) along the boundary due to an applied shear stress τ_i. (c) Distribution of normal stress (σ_{n_2}) along the boundary resulting from the presence of a normal (radial) residual stress (σ_R). [From Ref. 13]

When a shear stress τ_i and a normal stress σ_R are applied on the interface, an instantaneous elastic accommodation occurs at the interface, resulting in two superimposed normal stress distributions which vary periodically along the interface (Figures 12b and 12c). It was this varying local normal stress that was believed to drive diffusion controlled interfacial sliding. Funn and Dutta [Ref. 13] showed that the resultant average interfacial shear displacement rate could then be given by :

$$\dot{\bar{U}} = \frac{2D_m^{eff}\Omega\lambda}{kT\pi h^2}\left[\tau_i + \sigma_R\left(\frac{\pi h}{\lambda}\right)^3\right] + \frac{4\delta_i D_i\Omega}{kTh^2}\left[\tau_i + 2\sigma_R\left(\frac{\pi h}{\lambda}\right)^3\right] \quad (Eq.2)$$

where D_m^{eff} and D_i are the effective matrix diffusivity and interface diffusivity, Ω is the atomic volume of the diffusing matrix atoms, and δ_i is the thickness of the interface. The first term in $Eq.2$ represented the matrix contribution whereas the second term represented the interface contribution. In composites, the activation energy of interfacial diffusion is significantly smaller than that for matrix volume diffusion enabling the second term in $Eq.4$ to dominate and could be re-written, with the interfacial shear strain rate

$$\dot{\gamma} \approx \frac{4\delta_i D_i\Omega}{kTh^3}\left[\tau_i + 2\sigma_R\left(\frac{\pi h}{\lambda}\right)^3\right] \quad (Eq.3).$$

In the analysis of the data, three key points emerged from the experiment. First, interfacial sliding was adequately described by a continuum model based on the methods of Raj and Ashby [Ref. 35]. Secondly, the threshold stress was a direct function of the radial stresses acting on the interface. And finally, the activation energy for interfacial

sliding was quite low relative to the activation energy of volume diffusion in Pb. Based on the model and experiments, it was proposed that fiber-matrix interfaces undergo thermally activated sliding via diffusion-controlled creep with a threshold stress (Bingham flow).

This concept was expanded in Nagarajan et al. in which a Pb-Ni model SFC was fabricated that allowed direct measurement by a laser extensometer of the axial fiber displacements when axially loaded under a constant applied force using a lever-arm creep frame [Ref. 11]. A one-dimensional model was also developed for thermal cycling and axial creep of continuous fiber composites, accounting for diffusion-controlled interfacial sliding.

Both experimental and analytical results indicated that during creep or thermal cycling of continuous fiber reinforced composites, the matrix could elongate past the fibers resulting in a dimensional change between matrix and fiber. This occurred even when the sliding was confined to regions close to the sample extremities, as was the case when the fiber diameter was very small compared to the length of the composite. Thus, if interfacial sliding was present, the efficiency of the load transfer from the matrix to the fiber was decreased and the matrix no longer underwent relaxation completely via creep processes. The result was a reduction of the overall creep resistance of the composite causing significant differential strains leading to dimensional instability of the matrix and fiber even without interfacial fracture.

In an additional experiment by Dutta, the effects of thermal cycling on a rectangular cast 40 vol.% P100 Thornel graphite fiber reinforced 6061 Al composite were studied [Ref. 12]. In the experiment, the longitudinal thermal strain response of the

composite was measured during thermal cycles to 373 K and to 603 K. Results showed that the matrix protruded slightly beyond the fiber-ends after three thermal cycles to 373 K, while the fiber-ends protruded significantly beyond the matrix after three thermal cycles to 603 K.

From these experiments, it was clear that the matrix and fiber were not in an isostrain condition and since there appeared no direct evidence of interfacial fracture, again the differential strain between the matrix and fiber was believed to arise due to diffusionally-controlled interfacial sliding. A uni-dimensional micro-mechanical model for thermal cycling of continuous fiber reinforced metal-matrix composites was then developed in which the differential strains of the matrix and fiber were accommodated through diffusionally-controlled interfacial sliding from *Eq.*3 .

The model and experimental results were in good qualitative agreement and showed the significance of diffusionally-controlled interfacial sliding as a strain relaxation mechanism in a composite system where there exists a thermal mismatch. Hence, it was believed that diffusion-controlled interfacial sliding could have a direct impact on other material systems such as film-substrate systems with interfaces between dissimilar materials, as well as multi-phase alloys with inter-phase boundaries subjected to shear stresses.

Thus, in composite systems where two dissimilar materials with differences in their coefficients of thermal expansion are bonded together, significant shear and normal stresses can be induced when subjected to elevated temperatures. It is inferred from these experiments that in composites, and perhaps other material systems, these stresses may

result in diffusionally-controlled interfacial sliding whereby the matrix and fiber undergo permanent dimensional changes without interfacial fracture.

2. Microelectronic Devices

As discussed in section IIA, microelectronic devices are made by growing or depositing the various thin films onto a substrate of single-crystal silicon. Since many of these processes occur at elevated temperatures and because some of the materials have different coefficients of thermal expansion, very large thermal stresses are induced in these materials during manufacturing. Numerous studies have been conducted using substrate-curvature measurement, indentation, and x-ray analysis techniques to measure these induced stresses. However, few studies have been conducted to study the plastic deformation of thin films induced by thermal stresses.

One study by Chen and Dutta attempts to directly measure plastic deformation of thin films associated with thermal cycling through use of an atomic force microscope (AFM) [Ref 9]. In this study, physical vapor deposition was used to deposit 250nm thick, 6 μm x 6 μm pure Al films onto a Si (100) wafer covered by a Ni mask. The samples were subsequently subjected to 5 thermal cycles from 293 K to 623 K in a vacuum furnace.

The plastic deformation of the films induced by thermal cycling was conducted by measuring the cross-sectional profiles of the square films both before and immediately after thermal cycle through the use of an AFM at room temperature in air (Figure 13).

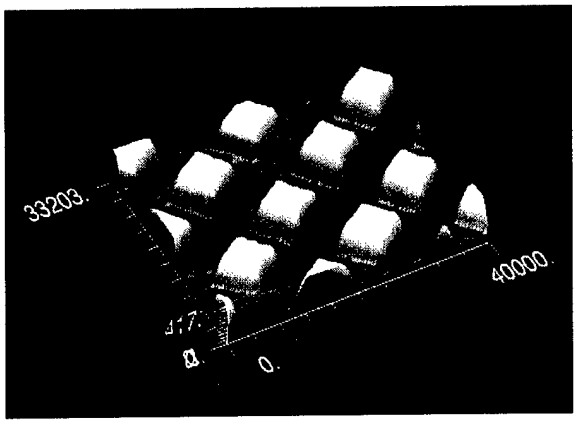

Figure 13: 40 μm x 33μm AFM scan of the Al films on the Si substrate [From Ref. 9]

Based on experimental data, the Al thin films were found to expand with respect to the Si substrate due to the thermal cycles (Figure 14). As observed, after thermal cycling, the film width close to the interface became larger and the slope of the film edges became sharper. This also suggested that a gradient of plastic deformation existed along the cross-section of the film, and that the majority of the plastic deformation occurred close to the interface.

(a)

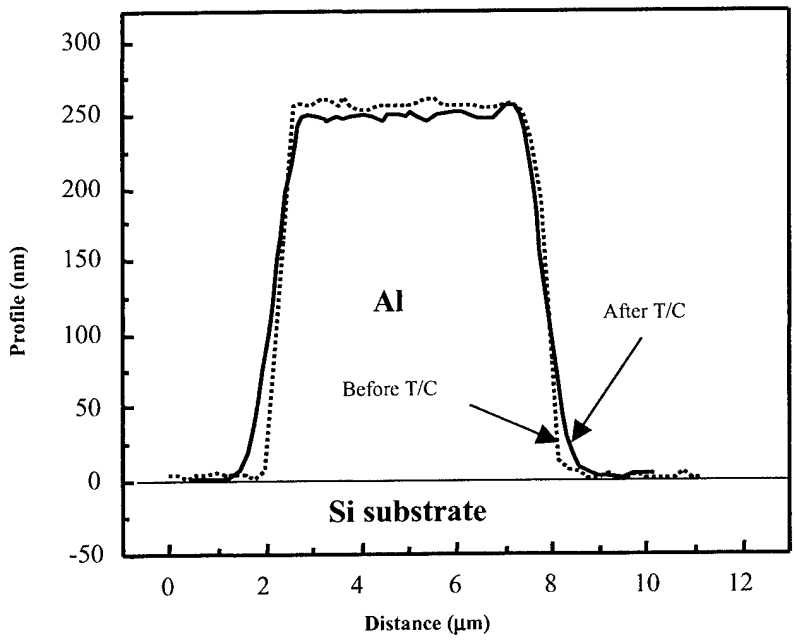

(b)

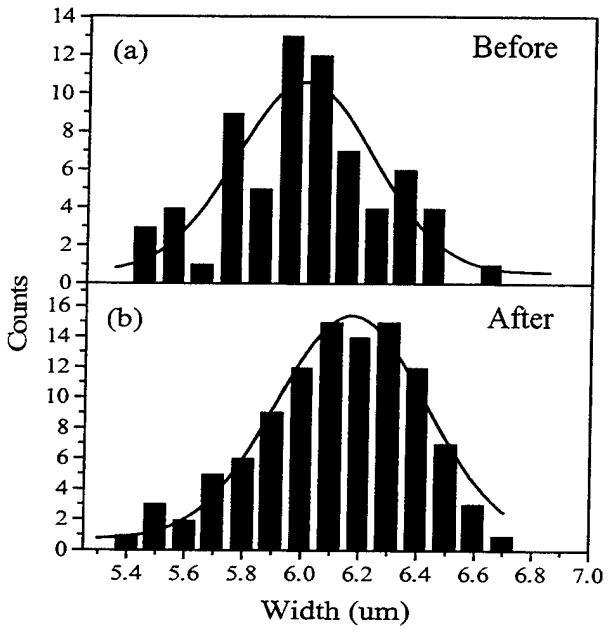

Figure 14: (a) Profile change and (b) width change in Al thin film [From Ref. 9]

Due to small amount of lattice dislocations and the difficulty of dislocation glide in thin films, plastic deformation via dislocation glide at low temperatures is likely to be limited during thermal cycling [Refs. 1,4]. Therefore, the dominant mechanism of plastic deformation of the thin film was believed to be creep/stress relaxation. Since the film is constrained by the Si substrate, permanent dimensional change between the Al film and Si substrate would not be possible unless interfacial sliding occurred. Thus, it was believed that near the edges of the film, creep relaxation of the film was accommodated by interfacial sliding due to the presence of interfacial shear stresses.

Further analysis of this experiment was conducted by Dutta et al. with the development of a plane-strain finite element (FE) model of a thin-film line on a Si substrate [Ref. 10]. The Si substrate was modeled as an isotropic elastic solid whereas the metallic thin-film was represented as an isotropic elastic-plastic-creeping solid exhibiting temperature dependent bilinear properties, and subject to dislocation creep via power-law (PL) and power-law breakdown (PLB).

Figure 15 shows the computed stress distribution along the film width in an unpassivated Al film following cooling to ambient after annealing at 644 K. Figure 15a plots the in-plane normal stress σ_{xx} very close to the interface ($y/t_f \cong 0.02$), while Figure 15b plots the interfacial shear stress τ_i at the interface ($y/t_f = 0$). In general, τ_i was maximum at the film edge ($2x/l_f = 1$), and decreased with increasing distance from the edge. In addition, Figure 15b shows that there was a normal stress (or peeling) stress, σ_{yy}, which was largest at the film edge and decreases rapidly upon moving away from the edge. It was this combination of interfacial shear stress and the normal peeling stress near the edges that was believed to drive stress relaxation via interfacial sliding. As noted in Figure 15, both τ_i and σ_{yy} are larger for smaller t_f/l_f values, and hence a narrower film was believed to display a greater degree of interfacial sliding.

(a)

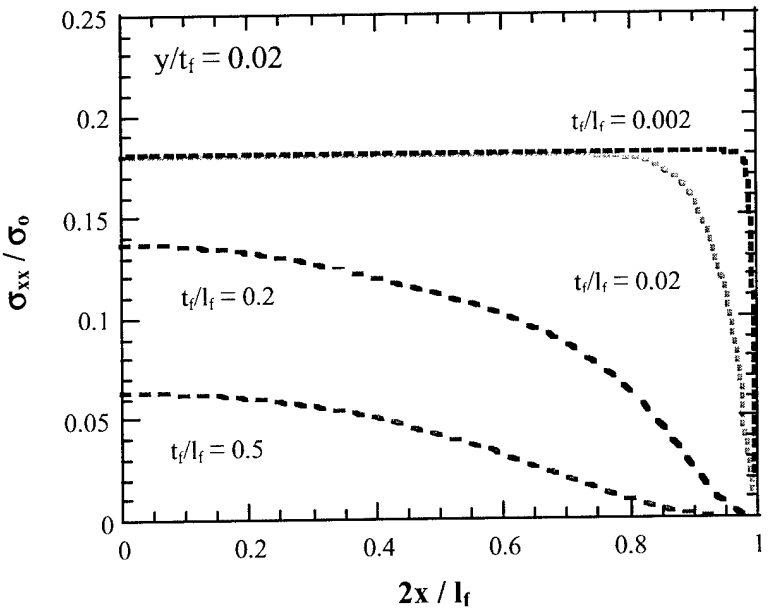

(b)

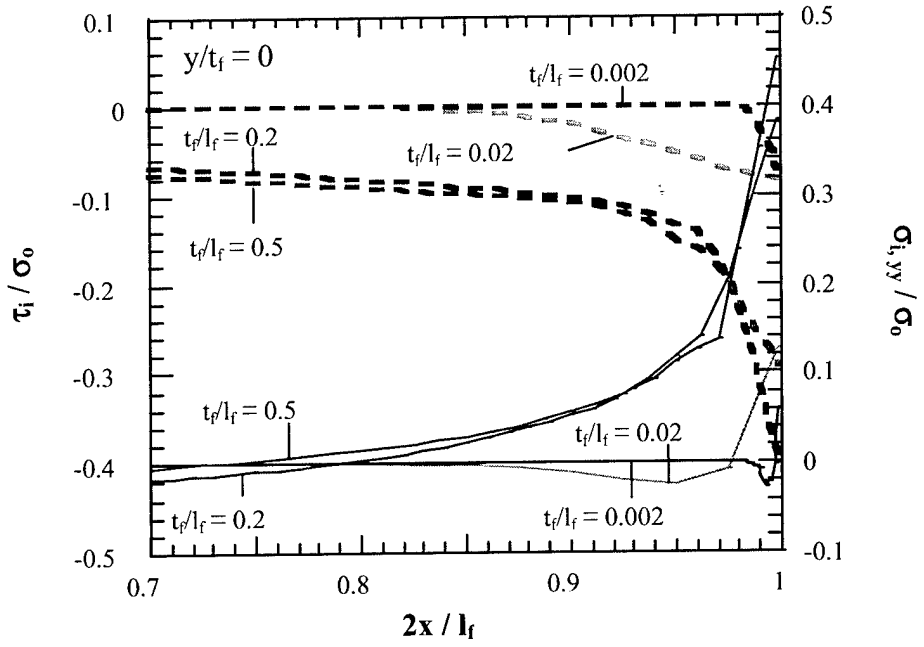

Figure 15: (a) Distribution of in-plane normal stress (σ_{xx}) along film-width for an Al film on Si at ambient temperature, following cooling from annealing temperature. (b) Distribution of interfacial shear (τ_i) and normal ($\sigma_{i,yy}$) stresses along film-width for the same conditions. The dashed lines refer to τ_i, while the solid lines refer to $\sigma_{i,yy}$.[From Ref. 10]

Figure 16 shows the computed variation of the maximum in-plane film stress at the centerline, $2x/l_f = 0$, and the midplane, $y/t_f = 0.5$, during thermal cycling following initial cooling from the annealing temperature. This model generally agreed with other stress analysis studies [Refs. 1, 5, 7- 8, 14,18, 26-28], and predicted that during one complete thermal cycle, the net plastic strain was tensile, and the net creep strain was slightly compressive. This resulted in a net inelastic tensile strain at the end of the cycle, which agreed with experimental results.

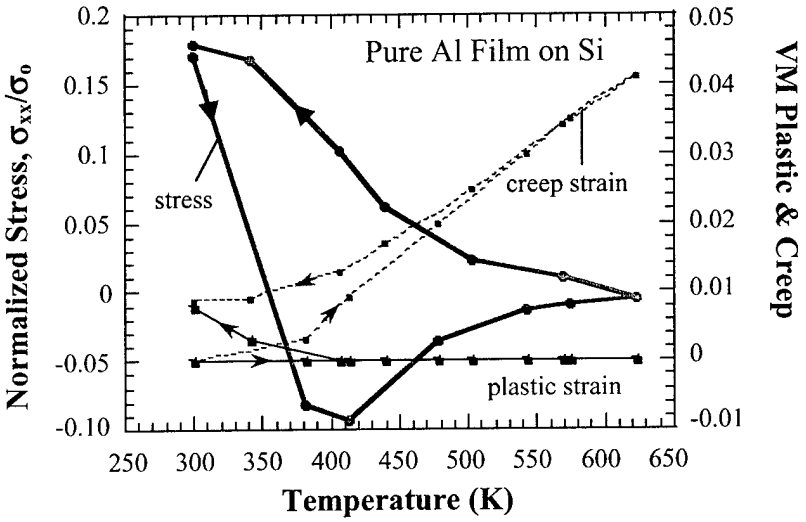

Figure 16: Computed variation of σ_{xx} and the Von-Mises effective plastic and creep strains in an Al film during thermal cycling. [From Ref. 10]

Both the experiment and model were in good agreement and showed the existence of large interfacial shear stresses near the edges of thin films which arise due to differences in the coefficients of thermal expansion between the film and substrate. Thus in the case of the evaporated Al thin films, both the normal peeling stress and the interfacial shear stress provided the driving force for diffusionally-controlled interfacial sliding causing both a size and shape change in the Al thin film in which it was also believed that smaller films could experience more of a change.

THIS PAGE INTENTIONALLY LEFT BLANK

III. OBJECTIVE

The purpose of this work is to modify the VISTA-100 atomic force microscope (AFM) to enable *in-situ* studies of plastic deformation and interfacial sliding of thin metallic films on Si substrates during thermal cycling in order to increase understanding of the reliability of integrated circuits.

To begin, *post-situ* results from direct measurement of the plastic deformation of thin Cu films on Si substrates induced by thermal cycling are presented to establish the need for detailed *in-situ* studies. This is accomplished through cross-sectional measurement of parallel 1.4 μm wide Cu films with a pitch of 2μm and a height of 200 nm before and after thermal cycling using the VISTA-100 AFM. Based on experimental results, the effect of film plasticity and interfacial deformation on the dimensional stability of thin metallic films is discussed.

Modification of the VISTA-100 Atomic Force Microscope consisted of the addition of a hot-stage for thermal cycling, a vacuum and purge system to provide a protective environment, and a cooling device to maintain a safe AFM operating temperature. The details of the design, along with the performance limitations of the system are discussed. In addition, preliminary results of an *in-situ* AFM study on a film-substrate sample are presented to demonstrate the performance of the system at an elevated temperature.

THIS PAGE INTENTIONALLY LEFT BLANK

IV. *POST-SITU* AFM ANALYSIS

A. EXPERIMENTAL APPROACH

The experiments were conducted using Cu-Si samples supplied by Dr. J. Molla of Motorola and a VISTA-100 Atomic Force Microscope for measurement. The Cu-Si samples consisted of a pattern of parallel 1.4μm wide Cu lines with a pitch of 2μm, a height of 200nm, and a length of 9mm. The Cu sides and ends were unconstrained. The Cu lines were deposited on a (100) Si wafer by lithographically patterning the lines in a photoresist spun on the wafer, sputter-depositing a barrier layer of Ta and a seed layer of Cu, followed by Cu electroplating, chemo-mechanically polishing the Cu for planarization, and completed with resist removal. The Si substrate had a length of 10mm, a width of 10mm, and a height of 0.75mm. The Ta interlayer had a height of 25-30 nm. Following deposition, the samples were annealed for 30 minutes at 673K to stabilize the Cu-grain structure. Figure 17 shows an SEM image of the Cu lines on Si substrate.

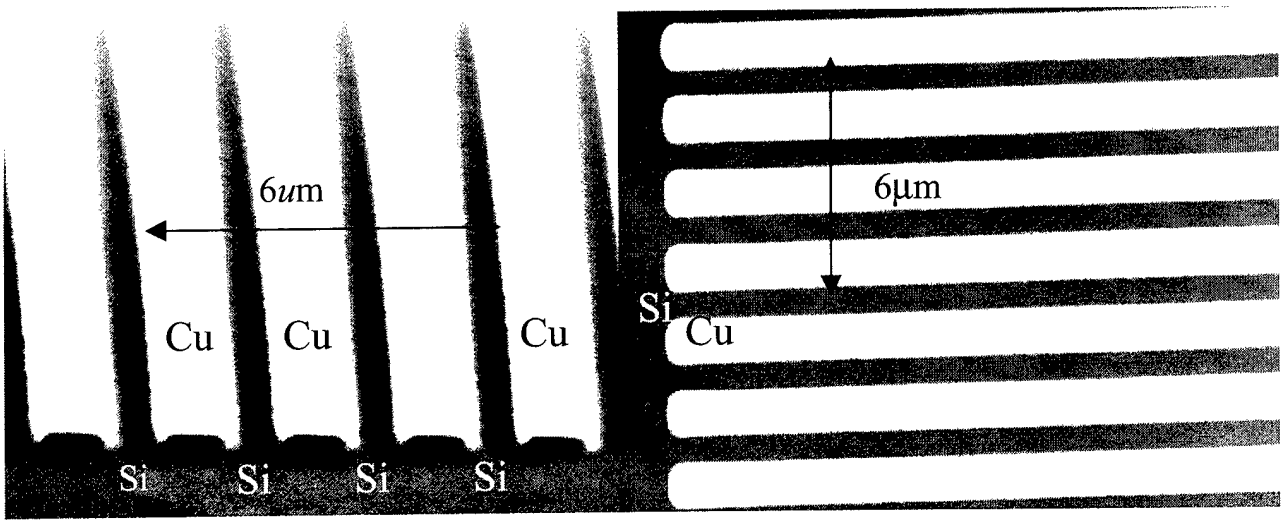

Figure 17: SEM images of Cu-Si film-substrate samples

Cross-sectional profiles of the Cu lines were then taken using a VISTA-100 atomic force microscope (AFM) in air at room temperature. The experimental scans were conducted in contact mode for increased accuracy, using a lateral scan size of 5μm x 5μm, a scan rate of 2Hz, and a pixel size of 512x512. Due to the dimensions and material strength, it was required to set the proportional gain control constant and force set point slightly higher than in normal AFM operation. The proportional gain control constant (adjusts signal gain) was set at 2.5, the integrator gain control constant (adjusts time constant) was set at 0.1, the feedback-loop cutoff frequency was set at 1000Hz, and the force set point for imaging was set at 30nN. Due to these settings and the completion of a background noise survey, the lateral displacement resolution produced was determined to be better than 10nm. Figure 18 shows a typical AFM image of the Cu lines on Si substrate over a 10μm x 10μm scan area.

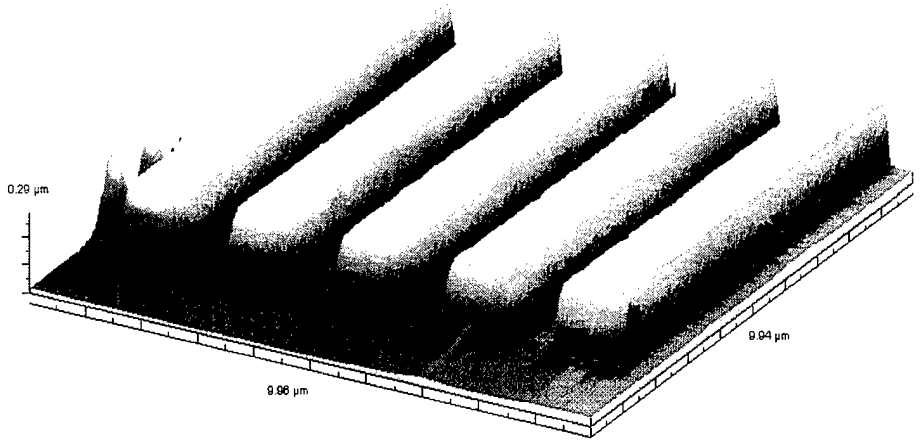

Figure 18: AFM image of Cu lines on Si substrate with a 10μm x 10μm scan size

The contact mode tips consist of a Nanosensors Pointprobe® CONT type sensor optimized for a high sensitivity by a low force constant [Ref. 37]. The probes consist of etched single crystal silicon with an integrated single crystal silicon tip. The tip is pointing into the <100> direction and the cantilever and tip are supported by a single crystal silicon holder. The typical specifications for a Pointprobe® CONT sensor are a cantilever thickness of 2μm, a mean width of 50μm, a length of 450μm, a Force Constant of 0.2 N/m, and a resonant frequency of 13 kHz. Figure 19 shows a Pointprobe® cantilever die assembly with its tip, cantilever, and holder assembly. Figure 20 shows a Pointprobe® tip and its pyramidal shape and polygonal base. The tip height is 10-15μm and has a cone angle at the apex of approximately 20°. This enables a tip diameter of better than 10nm. The cross-section of the cantilever is trapezoidal and is fixed to a silicon holder. In addition, an Al reflex coating approximately 30nm thick is deposited on the backside of the cantilever to enhance the reflectivity of the laser. The cantilever die assemblies are then attached to an Al cantilever tab using an electrically conductive epoxy by Thermal Centravision [Ref. 38].

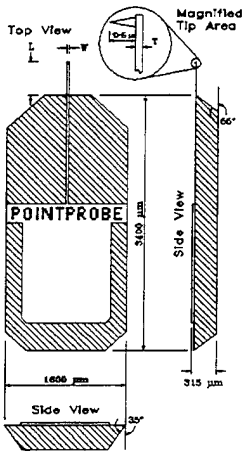

Figure 19: A Nanosensors Pointprobe® [From Ref. 37]

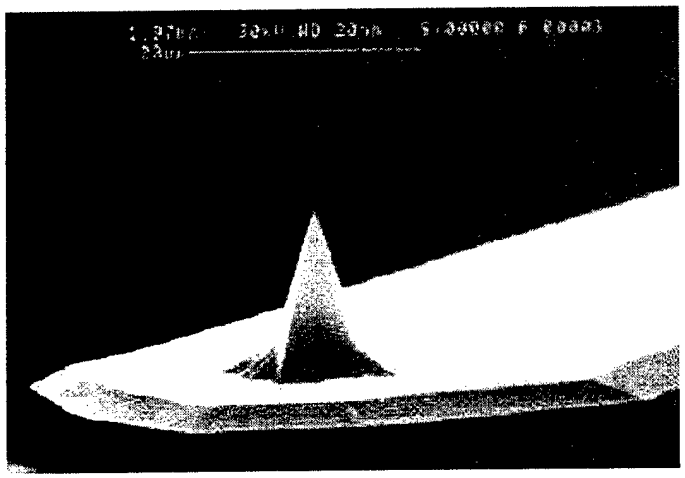

Figure 20: A Nanosensors Pointprobe® AFM sensor tip [From Ref. 37]

After the initial cross-sectional profiles of the Cu lines were taken, the samples were then placed in a vacuum chamber at approximately 1 x 10^{-7} torr. The samples were then heated from 293 K to 723 K at a nominal heating rate of 10 K/minute followed by a nominal cooling rate of 10 K/minute. The cooling rate from ~350K to 293K was uncontrolled but was nominally 1 K/minute. Heating and cooling was conducted using a mica heater powered by a dc voltage source. Cross-sectional profiles of the samples were measured after one, three, and five complete thermal cycles in air at room temperature.

B. EXPERIMENTAL RESULTS AND DISCUSSION

Figure 21 shows a typical cross-sectional profile and the change in width of the Cu films before and after the respective thermal cycles. Since there was some deviation in measured film width, at least 60 AFM scans were conducted after each respective thermal cycle. Generally, the film-width close to the interface becomes smaller and the slope of the film becomes steeper after thermal cycling.

(a)

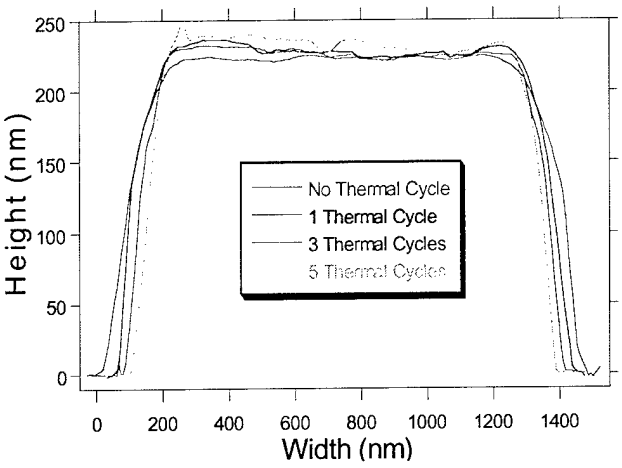

(b)

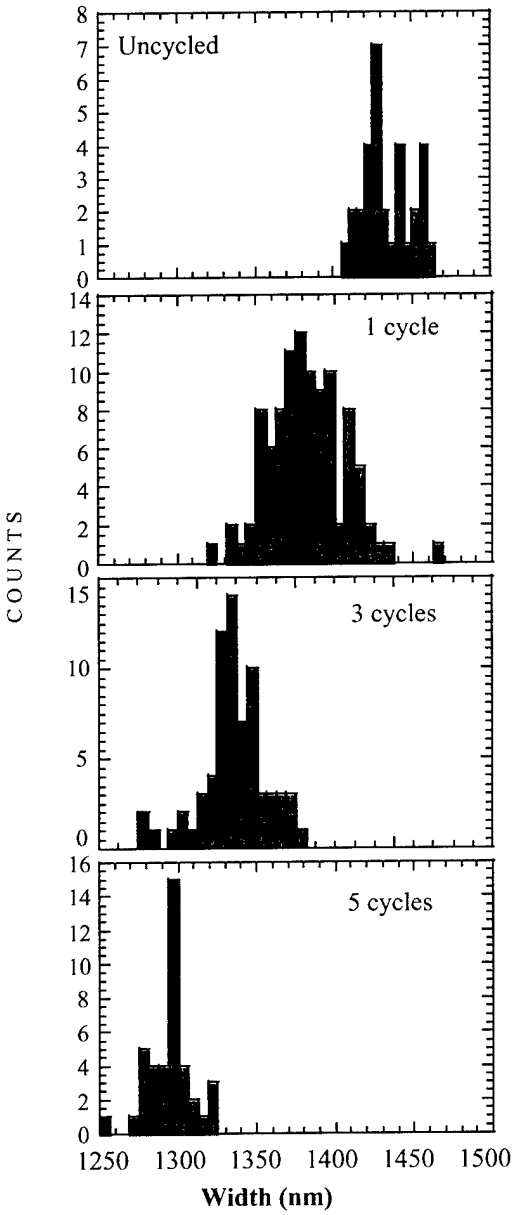

Figure 21: Cu line cross-sectional (a) profiles and (b) widths due to thermal cycling

As shown, the mean width decreased from 1.429μm before thermal cycling to 1.294μm after the 5th thermal cycle. Measured films widths were found to vary within a standard deviation (2σ) value of 0.013 to 0.022 μm, well below the measured change in line width due to thermal cycling.

Based on experimental data, it appears that due to the mismatch in the coefficients of thermal expansion, the Cu line widths are shrinking with respect to the substrate, with the majority of the deformation occurring close to the interface. Upon heating, since the copper thin film possesses a higher coefficient of thermal expansion, the copper thin films are placed in a state of compression. This can be visualized by first removing the film and substrate, allowing their dimensions to change based on thermal expansion, and then reattaching the film and substrate. Thus, the differences in thermal expansion will produce shear stress along the interface with the largest stress near the edges of the film.

Since thin films possess few lattice dislocations and since the substrate can constrain the movement of dislocations, plastic deformation via dislocation glide is unlikely. It is therefore assumed that high-temperature power-lower creep and lattice diffusion act as the primary stress relaxation mechanisms. However, with only these stress relaxation methods present, the film dimensions right next to the interface would not be able to change relative to the Si substrate. Thus, it is believed that in the absence of interfacial fracture, dimensional change between the film and substrate is accommodated by diffusionally-controlled interfacial sliding.

Based on physical properties, it would first appear that in comparison with the Al-Si film-substrate system studied by Chen and Dutta [Ref. 9], the Cu thin films should experience less of a proportionate dimensional change than the Al films due to copper's

slightly lower thermal expansion coefficient and its higher modulus. This contradicts our experimental results in which the Cu thin films have a larger proportionate plastic strain than the Al thin films. However, unlike evaporated Al, electroplated Cu has been observed to be nearly stress-free after annealing [Ref. 39]. In comparison with the Al films, it is believed that electroplated Cu thin films typically experience a compressive stress history throughout most of a thermal cycle. In addition, since the Cu films are much narrower than the Al films, diffusionally-controlled interfacial sliding is allowed to occur over a larger portion of the line width than for the Al films. Thus, as observed, the Cu thin films show the greater proportionate change in line width, where the driving force behind the interfacial sliding are the significant interfacial compressive stresses.

Similar to the Al-Si system studied by Chen and Dutta [Ref. 9], it is believed that the Cu lines also experience the phenomenon of diffusionally-controlled interfacial sliding. Thus, the use of Cu thin films will also require restrictive fabrication requirements. This is particularly important due to the current push in the microelectronics industry for smaller films to increase integration and the use of new dielectric films that have significantly lower elastic moduli than the traditional SiO_2. Thus, based on these *post-situ* results, the development of an experimental assembly to enable *in-situ* thermal cycling experiments is essential to increase the understanding of film-substrate effects and the reliability of microelectronic devices.

THIS PAGE INTENTIONALLY LEFT BLANK

V. DEVELOPMENT OF CONTROLLED-ATMOSPHERE CHAMBER WITH HOT-STAGE

A. REQUIREMENT

As discussed, various physical properties and experimental results can be determined or "imaged" on a nanometer scale using an atomic force microscope. In the case of plastic deformation of thin metallic films, although measurement before and after thermal cycling does aid in determining deformation history, it is very desirable to observe *in-situ* plastic deformation in a variable-temperature environment. Hence, through use of a hot-stage, one can map the plastic deformation of a thin film over a temperature history, and hence predict the reliability of a microelectronic device.

B. CONTROLLED-ATMOSPHERE CHAMBER

Due to oxidation reactions that can readily occur between thin metallic films and air [Ref. 42], and the fact that sound isolation and the elimination of air currents is crucial in attaining optimum resolution during Atomic Force Microscopy [Ref. 32], the construction of a controlled-atmosphere chamber is crucial to the accuracy of any variable-temperature AFM study.

Figure 22 shows the completed controlled-atmosphere chamber and assembly which was capable of an ultimate pressure of 1 torr. Successive evacuate and purge cycles could also be implemented in order to lower the oxygen content below 10 ppm so that no significant oxidation occurs. The basic construction began with the use of an 18in x 18in PYREX™ bell jar which is placed on a 20in x 20in x ½in thick 316 Stainless

Steel baseplate (Figure 23). A Viton® gasket is used as the sealing surface between the bell jar and baseplate.

Figure 22: Controlled-atmosphere chamber and assembly

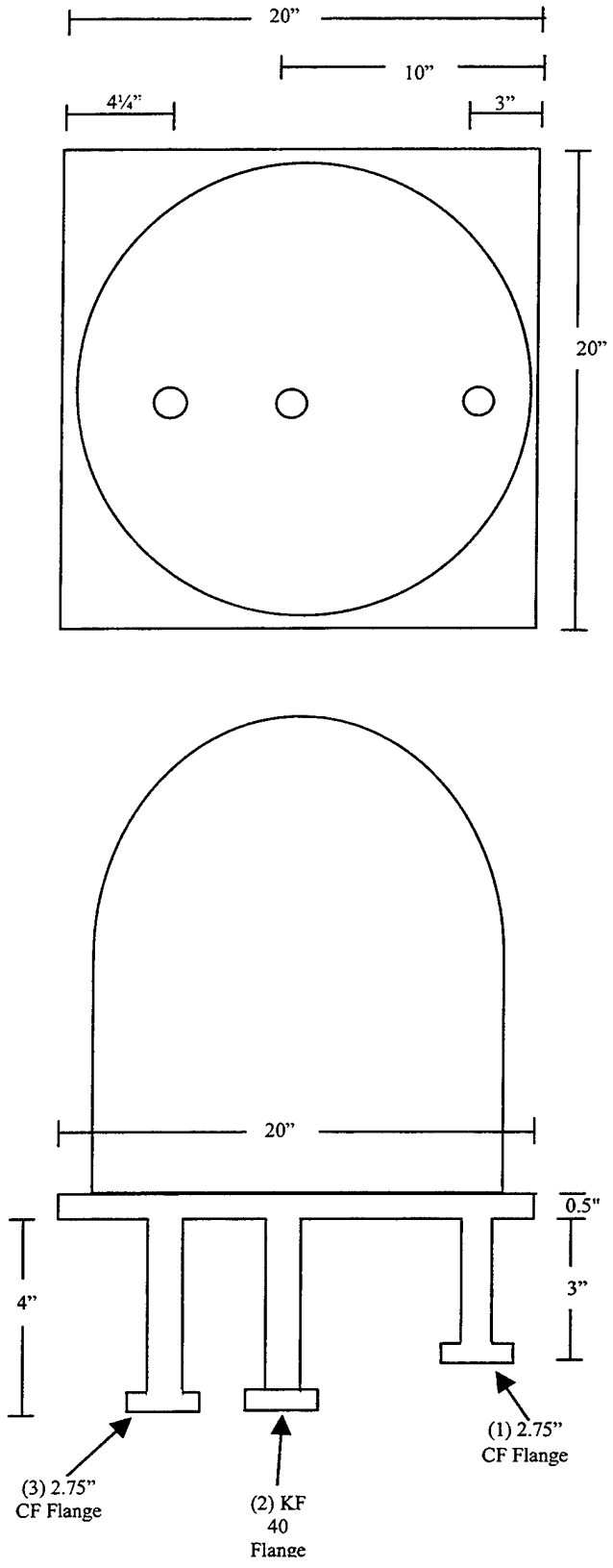

Figure 23: Bell Jar, SST baseplate and vacuum feedthroughs

The three vacuum feedthroughs consisted of tubing welded to the bottom of the baseplate for service connections. Feedthrough 1 consisted of an 1.5in OD, 0.065in tube wall, 3in length of type 304 Stainless Steel tubing with a 2.75in OD Del-Seal™ Conflat(CF) non-rotatable metal-seal flange welded to the tubing. Figure 24 shows the typical mated cross section of a CF metal-seal flange. Feedthrough 2 consisted of an 1.5in OD, 0.065in tube wall, 4in length of type 304 Stainless Steel tubing with a KF40 (Kwik-Flange™) flange welded to the tubing. Figure 25 shows the typical installation of a KF vacuum flange. Feedthrough 3 consisted of an 1.5in OD, 0.065in tube wall, 4in length of type 304 Stainless Steel tubing with a 2.75in OD Del-Seal™ Conflat (CF) non-rotatable metal-seal flange welded to the tubing.

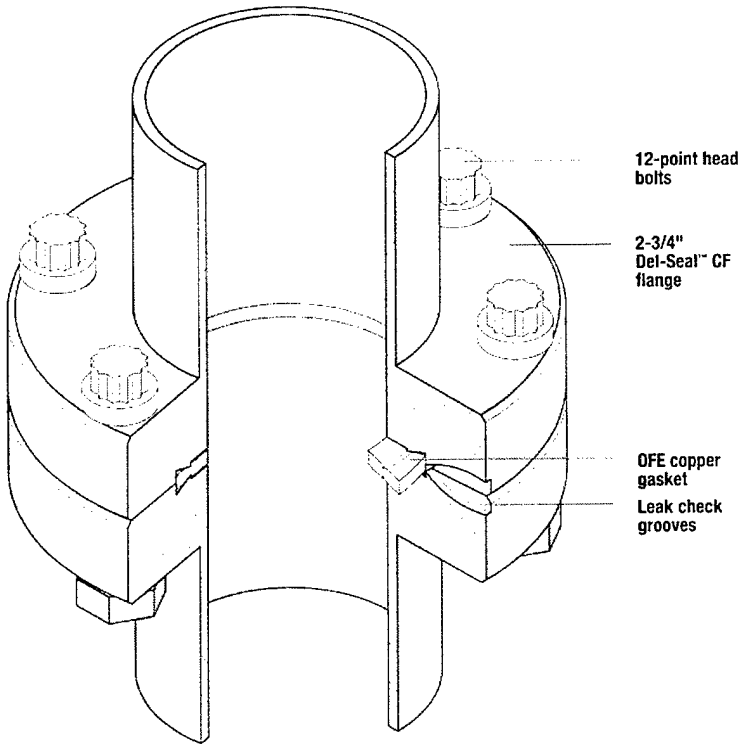

Figure 24: Typical installation of Del-Seal™ Flange [From Ref. 40]

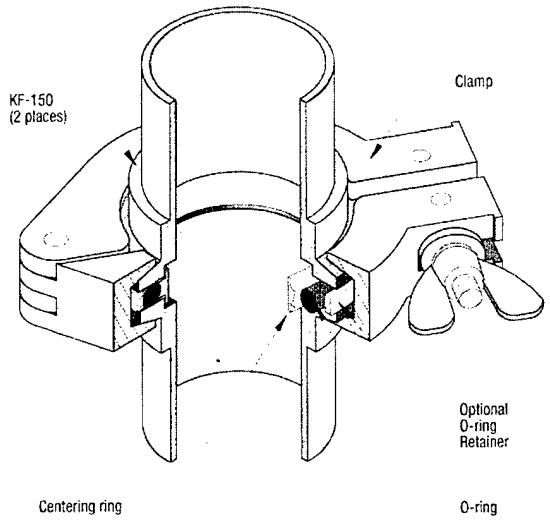

Figure 25: Typical installation of KF-type flange [From Ref. 40]

Feedthrough 1 was mated to another 2.75in OD CF-flange which had a 2.5 in length of 1in OD type 304 Stainless Steel tubing welded to the flange. This arrangement was utilized for the AFM scanning module cooling assembly shown in Figure 26, and was vacuum tested to approximately 1 x 10^{-2} torr using a roughing pump. The cooling assembly was designed as a simple cold finger, consisting of 1/4in dia. copper rod, a 3in x 3in x 1/32in copper plate, one copper washer, and four copper braids. Two sealing surfaces were required to effectively isolate the chamber. The inner sealing surface consisted of five size 009 o-rings which were seated into grooved notches on the copper rod. Grooved notches were used to eliminate any possible slipping of the o-rings during assembly/disassembly. The first o-ring was placed on the bottom surface of the copper washer while each additional o-ring was located at 1/2in intervals. The inner seal was made by placing the rod and o-rings into a 3/4in OD, 3/8in ID, 5in length of PVC piping. The outer seal was between the outer surface of the PVC piping and the inner surface of the 1in OD SST tubing. Four size 113 o-rings were placed on the outer surface of the

PVC piping and formed an effective seal with the 1in OD SST tubing. The simple assembly procedure consisted of first seating the PVC piping within the 1in OD SST tubing, connecting the SST tubing/CF flange to the CF flange of feedthrough 1, lowering the copper rod and o-rings into the PVC piping, and attaching the copper braids to the bottom of the copper rod with a 1/2in 4-40 screw. All surfaces, with the exception of the face of the copper plate, where insulated with standard spiral pipe wrap. The cooling characteristics of this assembly will be discussed in Section C.

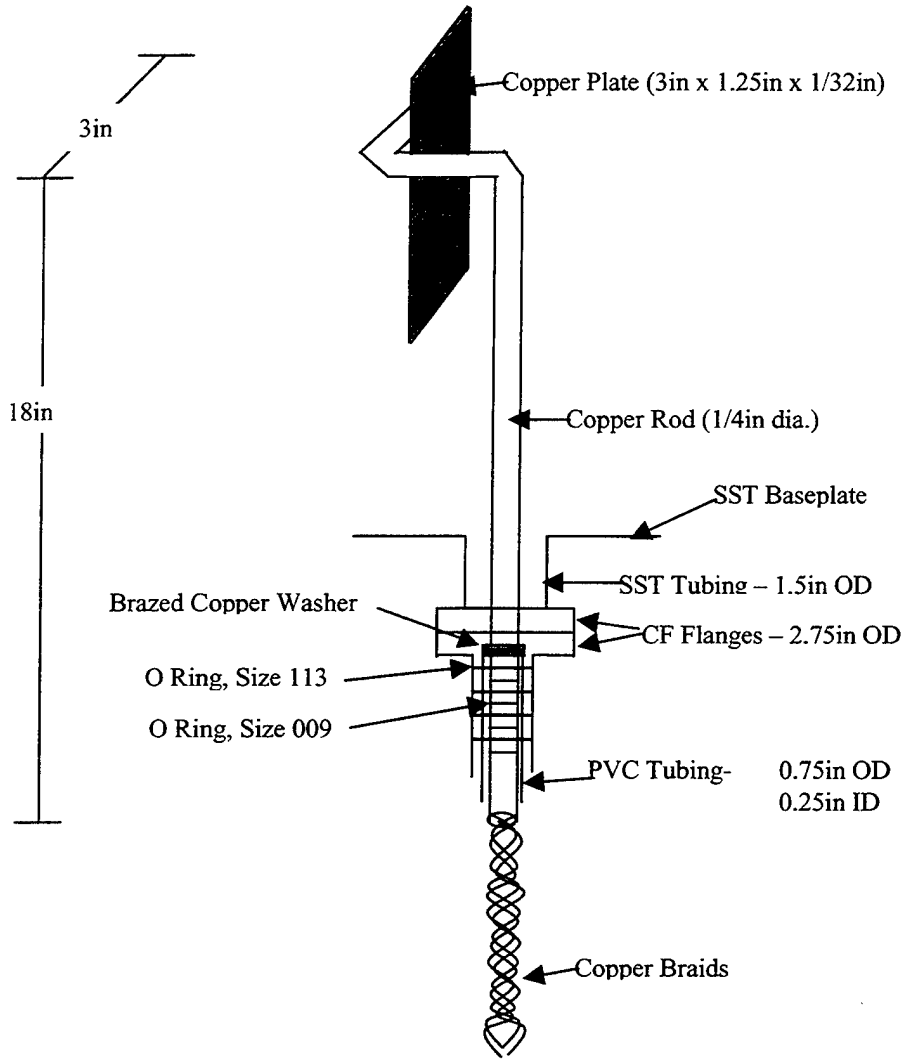

Figure 26: AFM scanning module cooling assembly (feedthrough 1)

Feedthrough 2 was mated with a 4-way KF40 cross and connected the primary vacuum control components as shown in Figure 27. The inline connection was mated to a KF40 to 2.75in OD CF adapter which was then connected to a hand-operated Varian® 1.5in right-angle SST valve which was used for system isolation. The valve was then connected to a 2.75in OD CF to KF40 adapter which was mated to a 1.5in spiraled SST reinforced vacuum hose. Connected to the vacuum hose was a Welch® Duo-Seal™ Model 1402 vacuum pump rated for a free air displacement of 5.6 cfm (160 L/min) and an ultimate pressure of 1×10^{-4} torr, and driven by a 115 V, 60 Hz, 1 PH, ½ hp General Electric motor. One side connection of the 4-way KF40 cross is mated to a KF40 stub with a single 1/4in NPT tapped hole and a 1/4in NPT thermocouple gauge tube threaded into the tapped hole. A Consolidated Vacuum Corporation Type GTC-100 thermocouple gauge tube and meter was used for vacuum measurement since it offers a fast and reliable means of measuring vacuum from 0.1 to 1000 micron HG (1×10^{-5} to 1 torr). The second side connection of the 4-way KF40 cross is also mated to a KF40 stub with a single 1/4in NPT tapped hole. A U.S. Gage Co. vacuum-pressure (Bourdon) gage rated to measure from 30 in Hg to 15 psig is connected to the stub through the use of standard NPT brass fittings and 1/4in copper tubing. Since it enables more accurate measurement than a thermocouple gage near atmospheric, the vacuum-pressure gage was useful when bleeding in argon or air into the chamber. Also included was a Varian® 1/8in NPT Up-to-Air Valve to control the addition of either argon, air, or other mixed gases. These components were all vacuum tested to approximately 1×10^{-2} torr using the Welch® vacuum pump.

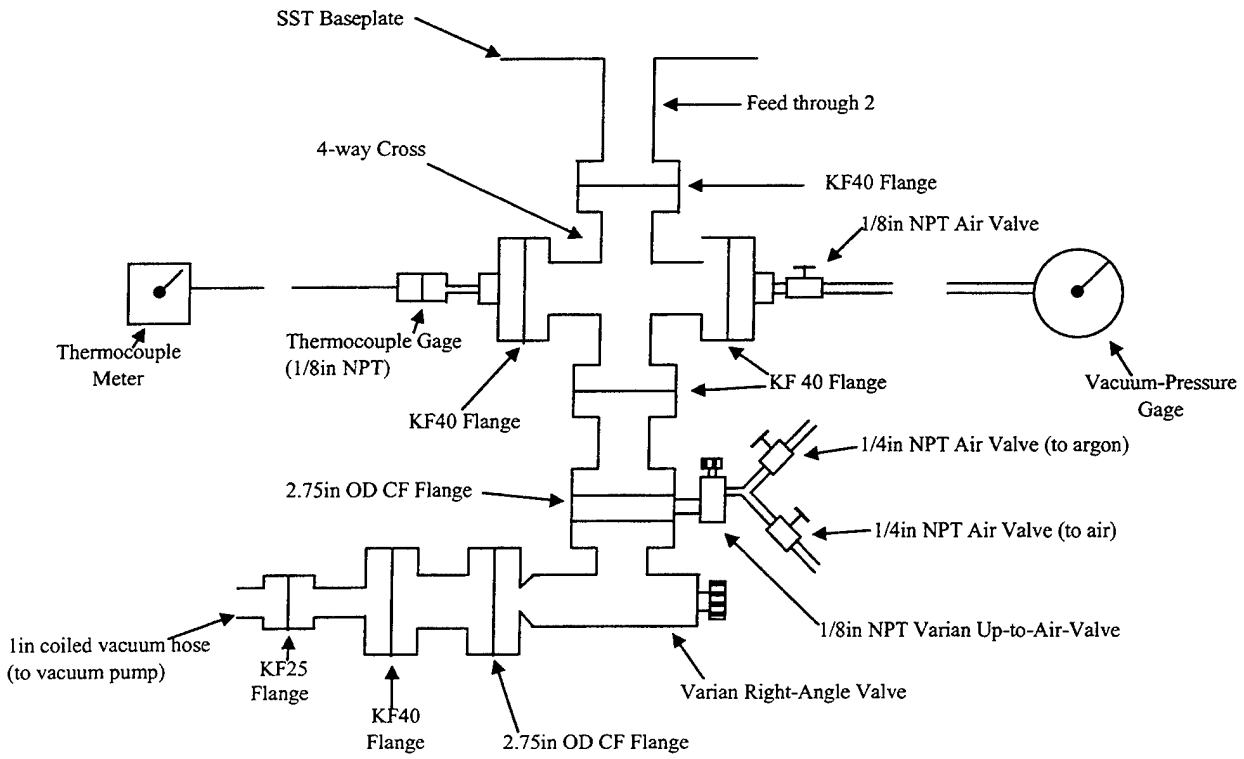

Figure 27: Feedthrough 2 and associated vacuum components and fittings

Feedthrough 3 was mated to an 8in OD CF Flange and was used for the various electrical feedthroughs required for the AFM and the hot-stage. The 8in OD CF Flange was connected to another 8in OD CF Flange on which a 4in OD, .083in tube wall, 6in length of Type 304 Stainless Steel tubing was welded. The purpose of the tubing was to house the Hawke® HRT100 Round Transit System for the electrical feedthroughs as shown in Figure 28. The eight electrical feedthroughs required were one 68-pin SCSI III cable, one 9-pin AWM 2464 high-voltage cable, one 24DC combined wire, one RG-174/U AWM 2990 camera-monitor cable, two size 28 thermocouple combined wires, and two 16-gauge heater wires.

(a)

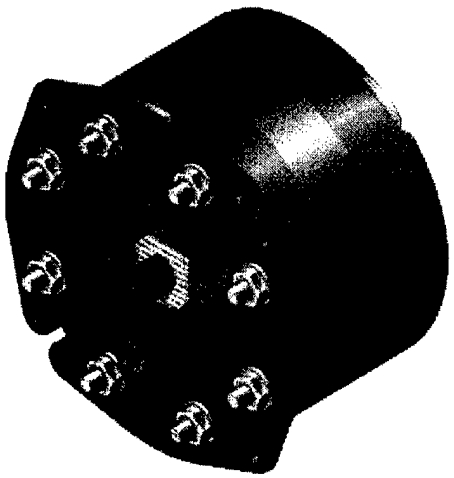

(b)

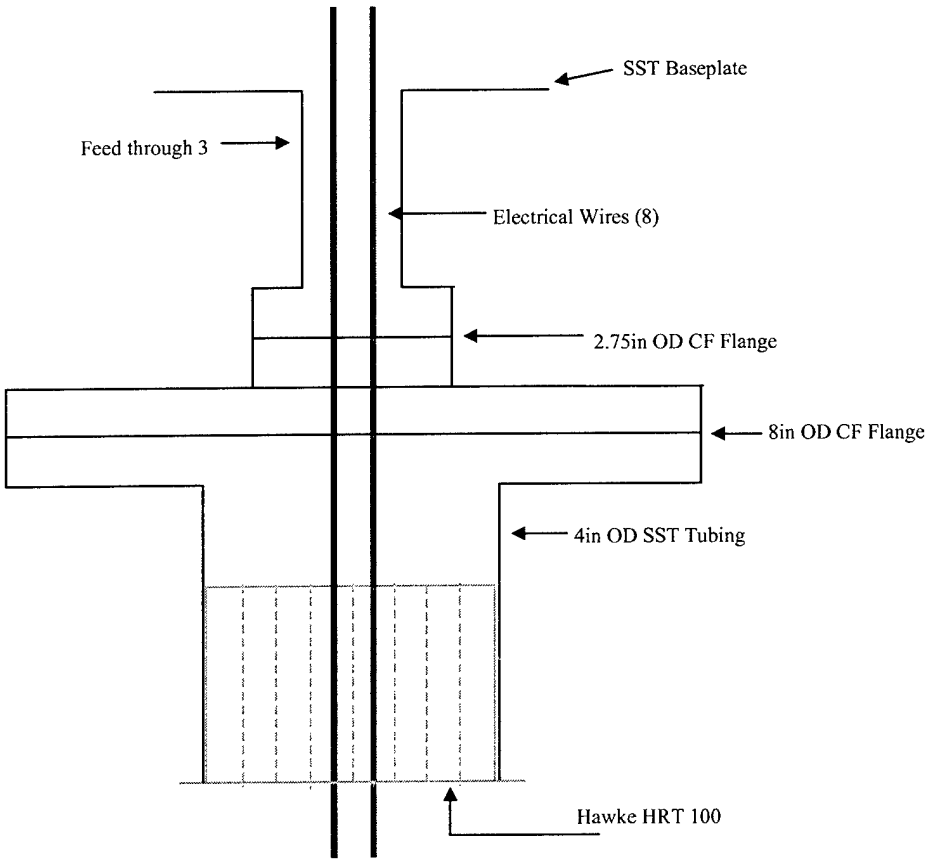

Figure 28: (a) HAWKE® HRT100, and (b) feedthrough 3

The HRT100 was selected for the electrical feedthroughs due to the very high cost of vacuum rated ceramic-to-metal electrical feedthroughs, especially for custom connections such as the 68-pin SCSI III cable and the 9-pin high voltage cable. The HRT100 is designed to effectively seal cables and pipes passing through circular apertures, and pressure seal against gas to a pressure of 50 psi. The seal is formed by tightening the compression bolts, which expands the system radially and causes pressure to be exerted against the aperture wall while closing down on the tolerant insert blocks. The appropriate tolerant insert blocks were selected based on wire diameter. To increase their vacuum capability, the tolerant blocks and wires were bonded using Varian® Torr Seal low vapor pressure resin. All other mating surfaces were coated with Dow Corning® high vacuum grease before assembly.

After assembly, the electrical feedthrough components were vacuum tested to 1 torr using the Welch® vacuum pump. Using a Veeco® MS-9 Helium Leak Detector, the location of the leaks was determined to be through the cables' insulation. Since the leaks were through the electrical wiring and not the HRT100, the current design did not allow for any further reduction in vacuum pressure. However, despite the loss of a satisfactory vacuum pressure, successive evacuation and argon bleed cycles could be conducted to lower the oxygen levels to acceptable levels to prevent oxidation of thin metallic films.

C. HOT-STAGE AND COOLING ASSEMBLY

The prospect of controlling sample temperature while simultaneously imaging a material extends the potential of any microscopy. However, since an atomic force microscope is designed to operate at ambient temperatures, the construction of a hot-

stage poses a number of challenges. Temperature and electrical transients need to be adequately controlled so that their effects on such devices as the PZT, tip, and laser do not affect AFM accuracy and/or control. In addition, many components of the scanning module may suffer physical damage at elevated temperatures. The design and operation of the hot-stage thus focused on safely elevating sample temperature while retaining AFM resolution.

The basic design of the hot-stage is shown in Figure 29. The main part of the assembly is the heater, which is a standard commercially available TEMPCO® channel strip heater with dimensions 1.5in(L) x 5/8in(W) x 1/4in(H). The size of the heater was the critical factor in order to limit the amount of excess heat transferred to the AFM scanning module. The 120V strip heater was rated at 50 Watts, with a 29 W/in^2 watt density, and a heated length of 0.50in. The basic design of the heater consists of helically wound nickel-chrome resistance coil evenly strung through ceramic insulator with all voids densely packed with magnesium oxide to increase thermal conductivity and dielectric strength. The outer sheath is Type 304 Stainless Steel providing both strength and dependable sheath temperatures up to 650°C. Either an ac or dc voltage source could be employed for heater use, with stability of the power source being the key factor in successful operation. With a 120Vac voltage source, automatic temperature control was achieved through the use of an OMEGA® CN4801 1/16 DIN fuzzy logic controller. With a dc voltage source, manual temperature control was employed by adjusting the voltage of a KEPCO® JQE-100 0-100Vdc power supply.

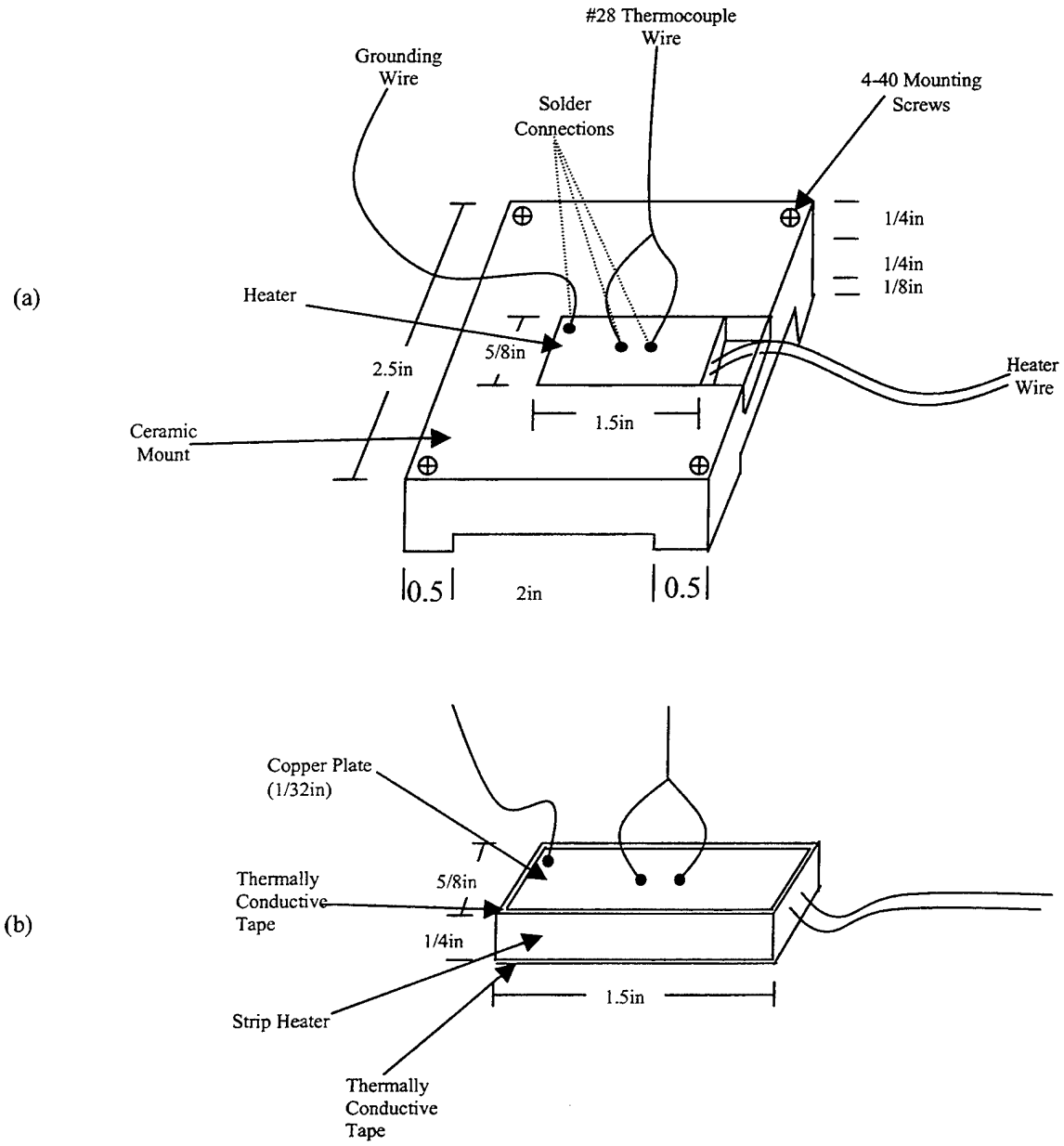

Figure 29: (a) Heater assembly and (b) heater

The heater was mounted in a machinable ceramic which could be easily attached to the millimeter sample stage of the VISTA-100 AFM through the use of 1in 4-40 mounting screws. The ceramic mount was designed for both ease of handling and to limit the amount of heat conducted to the AFM. The heater was bonded to the ceramic

mount with 3M® 9890 thermally conductive adhesive transfer tape. Maintaining its adhesive strength up to approximately 300°C, the transfer tape enabled a quick, high-strength, semi-permanent bond. Dow Corning® 340 heat sink compound also proved adequate as a bonding substance, although it remained stable only to approximately 200°C. Since there were minor temperature variations along the strip heater outer sheath, a 1/32in plate of copper was also attached to the top of the heater with the transfer tape. The sample could then be easily fixed to the copper plate through the use of the adhesive transfer tape or heat sink compound. Since the AFM often proved unstable due to the electric potentials between the tip and the heater when ungrounded, a grounding wire was solder-connected to the copper plate to aid in AFM stability.

Temperature measurement of sample and AFM was obtained using K-type thermocouples with No. 28 gage thermocouple wire and digital thermocouple meters. K-type thermocouples were used since they can accurately measure a wide range of test temperatures. In monitoring sample temperature, the positive and negative legs of the thermocouple were attached to the copper plate with a high-temp solder as shown in Figure 29. An intrinsic connection vice a spot connection was used in order to maintain a level mounting surface for the sample, with the separation distance between the positive and negative legs varied according to sample size. In monitoring AFM scan module temperature, the thermocouple was attached as close to the tip as possible, with the connection placed beneath the probe clip mounting screw (Figure 30). Figure 31 is the basic schematic diagram of the electric wiring and temperature measurement for the AFM and hot-stage assembly.

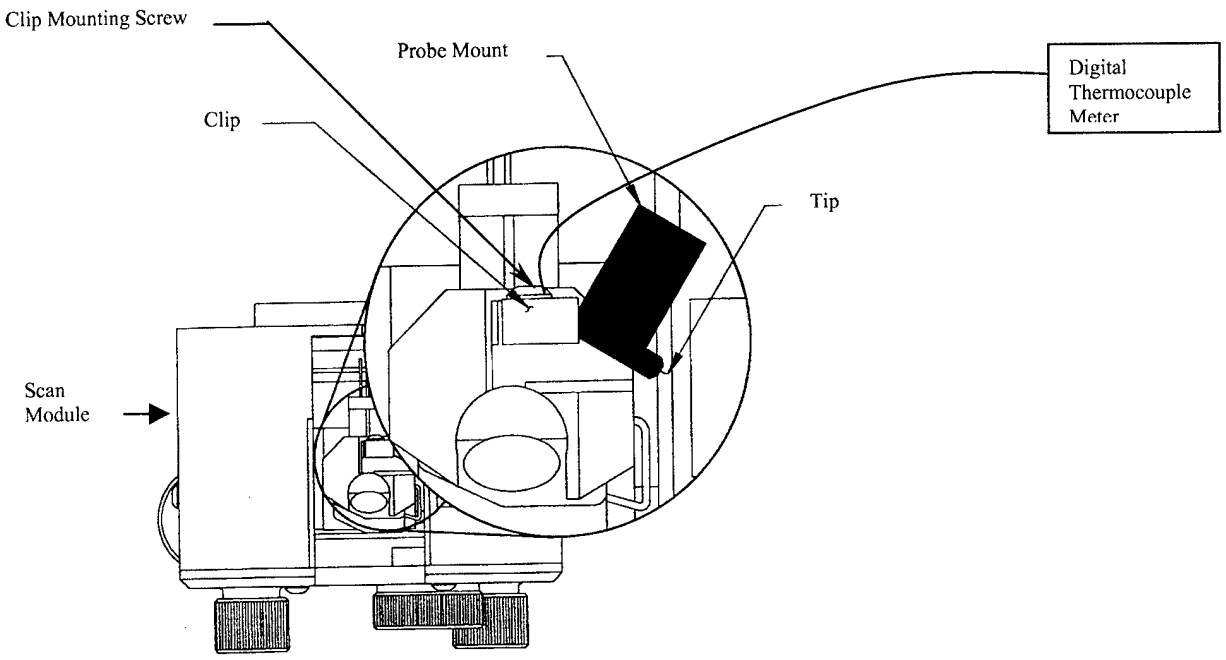

Figure 30: AFM scan module thermocouple attachment

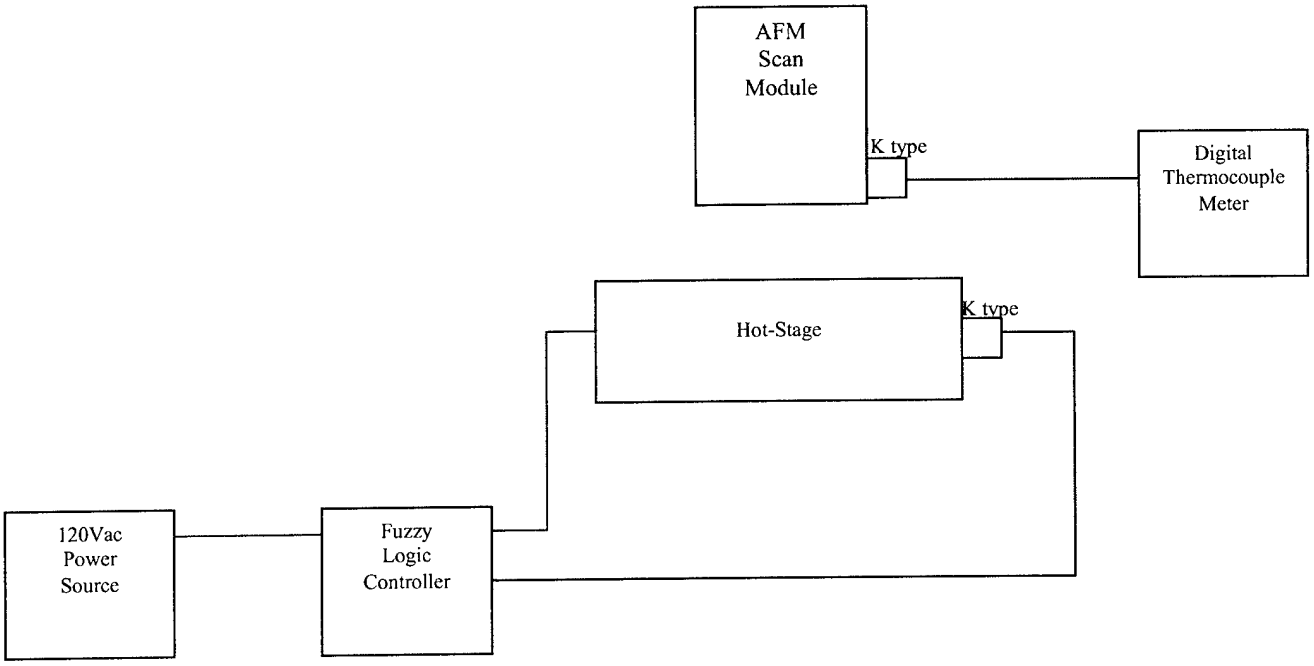

Figure 31: Schematic diagram of electric wiring and temperature measurement

As mentioned earlier, AFM scan module components such as wire sheaths, solder connections, and control circuitry are not designed to operate at temperatures greater than 100°C [Ref. 43]. As shown in Figure 42, a simple cold finger cooled by liquid nitrogen was employed, whereby a conductive heat transfer path between the cooled copper plate and the scan module aluminum casing would keep the temperature of the scan module under 100°C. The actual cooling of the cold finger was carried out by placing the copper braids into a liquid nitrogen dewar. The cold finger temperature could be grossly adjusted by adding varying amounts of liquid nitrogen and methanol to the dewar. This simple design was utilized due to the inherent sensitivity of scan module components to such cooling methods as thermoelectric or forced-flow cooling.

THIS PAGE INTENTIONALLY LEFT BLANK

VI. PERFORMANCE OF CONTROLLED-ATMOSPHERE CHAMBER WITH HOT-STAGE

A. EXPERIMENTAL APPROACH

The experiments were conducted using a NT-MDT® TGZ02 silicon calibration grating. The calibration grating consists of an active grating array of 3mm x 3mm with step heights of 100nm and a pitch of 3.0μm as shown in Figure 32. The TGZ02 is primarily intended for Z-axis calibration and nonlinearity measurements with an accuracy of step heights of 1.5nm. Although not specifically manufactured for lateral calibration, the TGZ02 does offer a grating that is very similar in design to many metallic thin films, making it a good test sample. The TGZ02 is composed of single crystal silicon with SiO_2 steps, while the whole grating is coated with a thin 10nm film of silicon nitride, Si_3N_4. The TGZ02 was selected as the test sample not only because of its dimensional tolerances, but also due to the fact that the SiO_2 steps were not assumed to vary during minor thermal cycles because of a low thermal expansion coefficient. This allowed a confidence check of the AFM during scanning at elevated temperatures.

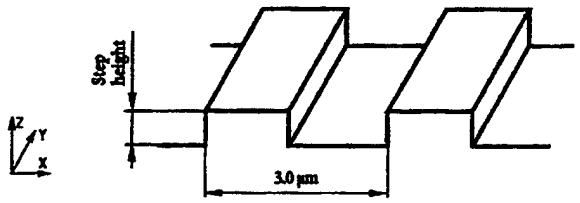

Figure 32: NT-MDT® TGZ02 calibration grating

Although the calibration grating is not as susceptible to oxidation as metallic thin film test samples such as the Cu-Si film-substrate systems, a controlled atmosphere was still initiated to represent thin film testing conditions. As stated, due to the electrical

feedthroughs, the controlled atmosphere chamber was capable of a vacuum pressure of only 1 torr. Due to this relatively low vacuum pressure, successive evacuation and argon fill cycles were initiated to lower the oxygen content to acceptable testing levels. The test level is based on the composition of the test sample but a good rule of thumb is to maintain 10ppm oxygen, which is sufficient to limit any measurable oxidation on the Cu-Si film-substrate systems [Ref. 14].

Once a controlled atmosphere was established, cross-sectional scans of the calibration gratings were taken using the VISTA-100 AFM *in-situ* at room temperature, 50°C, and 100°C. The thermal cycles consisted of heating the samples to the desired temperature at a nominal heating rate of 20K/min. The actual cross-sectional profiles consisted of measuring a total of five profiles, or 15μm, to illustrate the worst-case accuracy of the AFM during the thermal cycles. The experimental scans were again conducted in contact mode for increased accuracy, using a lateral scan size of 20μm x 20μm, a scan rate of 2Hz, and a pixel size of 512x512. The proportional gain control constant was set at 2.5, the integrator gain control constant was set at 0.1, the feedback-loop cutoff frequency was set at 1000Hz, and the force set point for imaging was set at 30nN. A background noise survey revealed that there was no measurable background noise affecting the AFM scans when inside the controlled atmosphere chamber. Therefore, resolution was a function of scan size and pixel size and was thus determined to be better than 20nm.

B. EXPERIMENTAL RESULTS AND DISCUSSION

Figure 33 shows a typical AFM cross-sectional scan at room temperature and a

typical cross-sectional profile. Forty length and height measurements were taken with an average 5-pitch length measurement of 14985.46nm and an average step height measurement of 98.89nm. Length measurements were within a standard deviation of 0.033μm and height measurements were within a standard deviation of 0.001μm. Thus, despite the relatively low resolution, the AFM shows exceptional accuracy of both the calibration grating height and pitch dimensions.

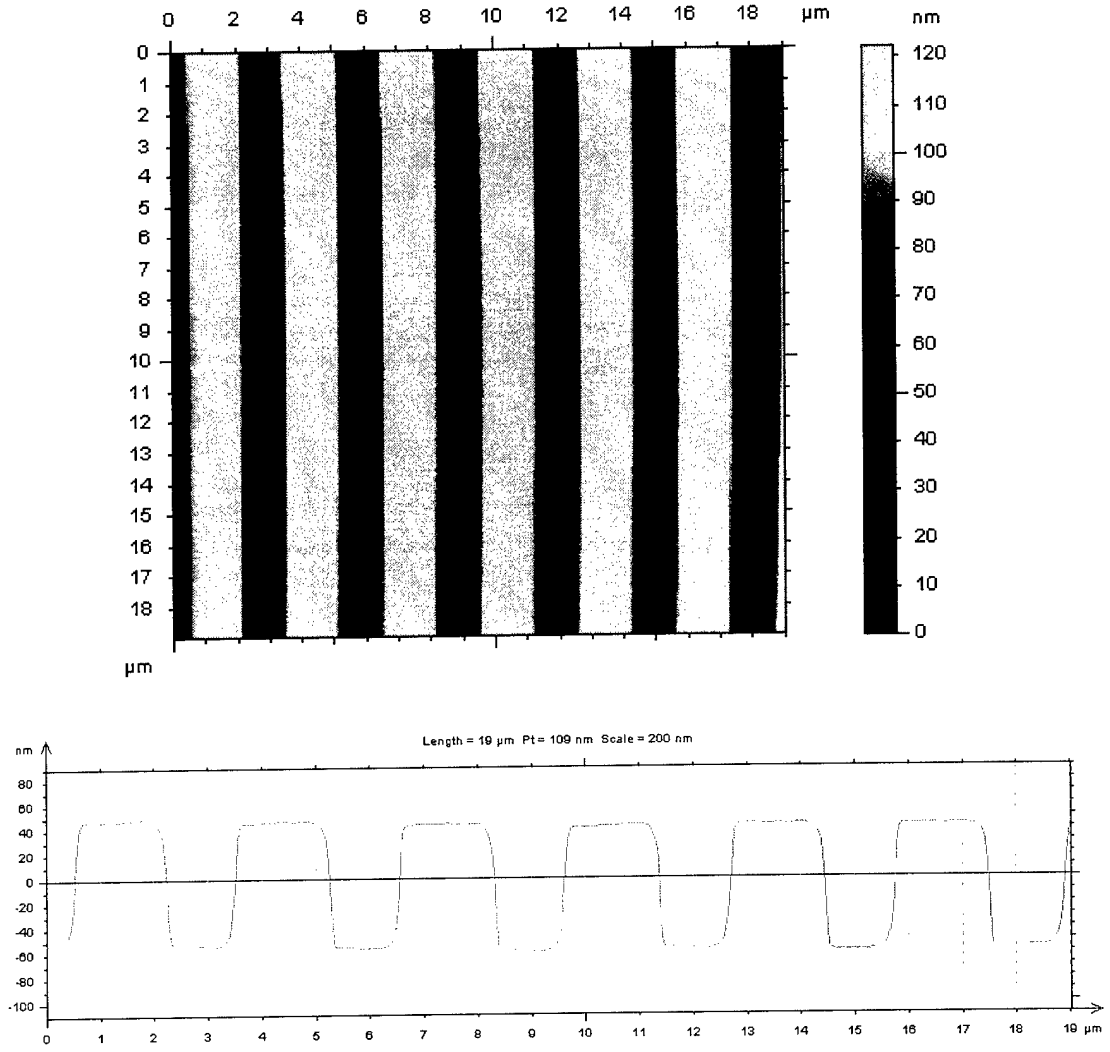

Figure 33: Room temperature AFM scan and line profile of calibration grating

The samples were then heated to 50°C with the AFM scan module in the raised position. The heater and controller assembly were able to maintain sample temperature within ± 0.1°C. Once the desired temperature was achieved, the AFM scan module was lowered into the engaged position. The tip was left in the engaged position for a minimum of five minutes prior to scanning to ensure sample and probe thermal equilibrium. Sample and probe thermal equilibrium proved a necessity since the Nanosensors Pointprobe® with the reflex coating was observed to bend and twist during thermal instabilities. The bending of the tip could be visually verified with the AFM video camera, and was assumed to be due to the thermal mismatch between the silicon cantilever and tip, and the aluminum reflex coating. The tip was often physically damaged or proved unreliable if thermal equilibrium within ± 0.1°C was not maintained as shown in Figure 34.

(a)

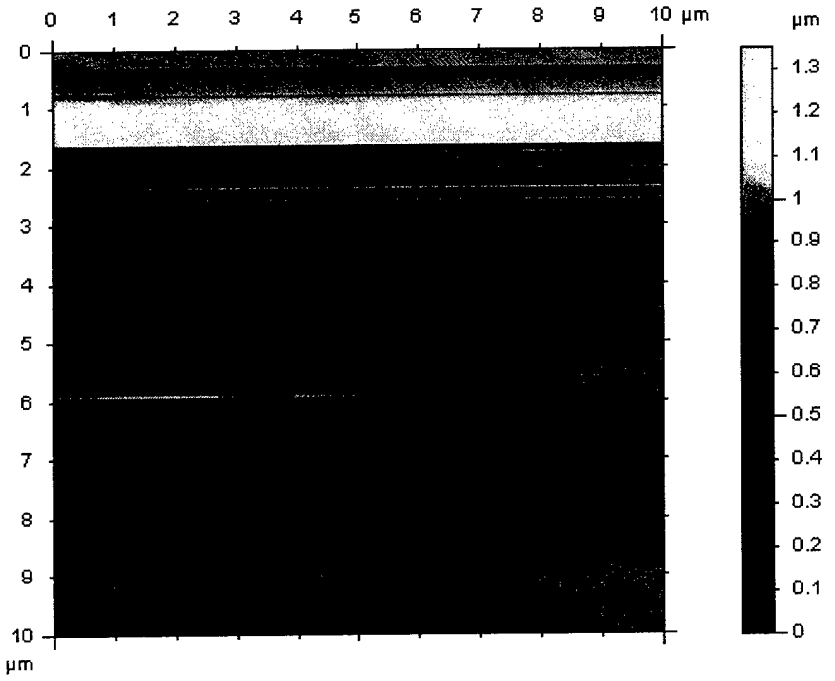

(b)

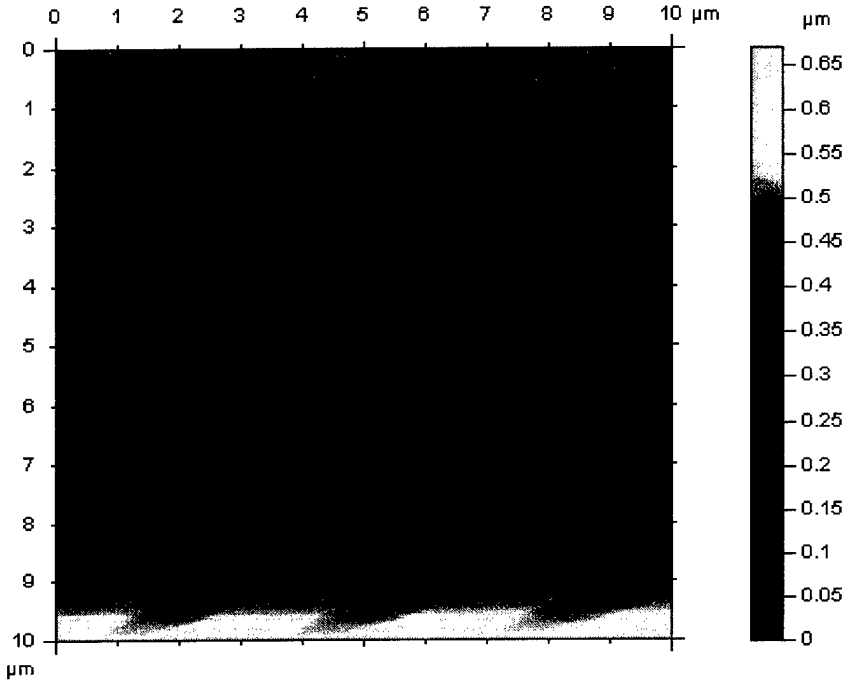

Figure 34: AFM scans with temperature varying >± 0.1°C showing (a) a damaged tip, and (b) an unreliable tip

Figure 35 shows a typical AFM cross-sectional scan at 50°C and a typical cross-sectional profile. As observed, even with a temperature variation of within ±0.1°C, there is some difference in the baseline of the scan height, with the lighter regions representing an increase in temperature and the darker regions representing a decrease in temperature. However, when conducting cross-sectional profiles in all regions of the scan, there was no difference in either length or height data. Thus, a cross-sectional profile represents a region of relatively minor temperature change at that particular instant. In this case where a pixel size of 512x512 and a scan rate of 2Hz is used, each cross-section represents a time of approximately half a second. The minor temperature change, although affecting the AFM's reference height, does not appear to significantly affect its

cross-sectional data. Although not directly relevant to this experiment, minor pressure variations produced similar scan results as those due to temperature variations. Again, forty length and height measurements were randomly taken with an average 5-pitch length measurement of 15006.32nm and an average step height of 98.76nm. Length measurements were within a standard deviation of 0.035μm and height measurements were within a standard deviation of 0.001μm. Of note, the maximum temperature of the AFM scan module as measured by the attached thermocouple was 34.4°C.

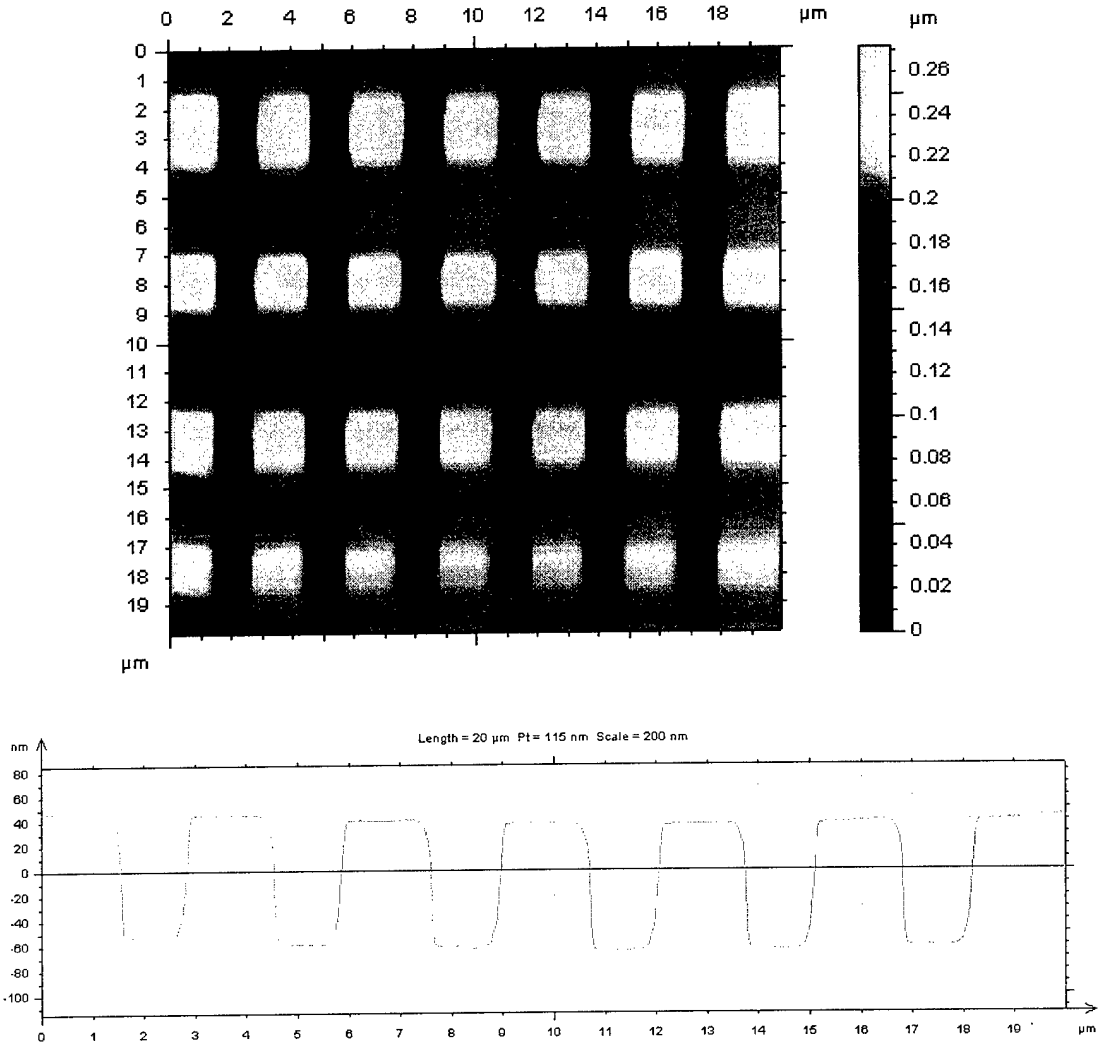

Figure 35: (a) 50°C AFM scan and (b) line profile of calibration grating

The samples were then heated to 100°C with the AFM scan module again in the raised position. Once the desired temperature was achieved and maintained within ±0.1°C, the scan module was lowered into the engaged position and left for a minimum of five minutes to ensure thermal equilibrium. Figure 36 shows an AFM scan at 100°C and a cross-sectional profile. As observed, there is a skew present in both the scan and profile in addition to the minor temperature variation. This is shown to highlight the importance of aligning the sample and AFM prior to conducting the scan when attempting to compile accurate cross-sectional data during elevated temperature scans. This can be achieved by taking care in mounting the sample and using the appropriate AFM angle offset to exactly align the sample perpendicular to the scan direction. Again, forty length and height measurements were randomly taken on appropriately aligned scans with an average 5-pitch length measurement of 14992.56nm and an average step height of 100.46nm. Length measurements were within a standard deviation of 0.031μm and height measurements were within a standard deviation of 0.001μm. Of note, the maximum temperature of the AFM scan module as measured by the attached thermocouple was 49.2°C.

At 100°C, even when a stable temperature was maintained and the sample and tip were allowed to reach thermal equilibrium, proper laser alignment proved more challenging. With the corresponding increase in temperature of the AFM scan module, the laser was observed to drift slightly. This was assumed to be due to expansion of the mechanical connections of the laser alignment mirrors. Although with adequate control the laser maintained proper alignment with the split detector, further increases in

temperature may prove difficult to maintain the alignment necessary for accurate scanning.

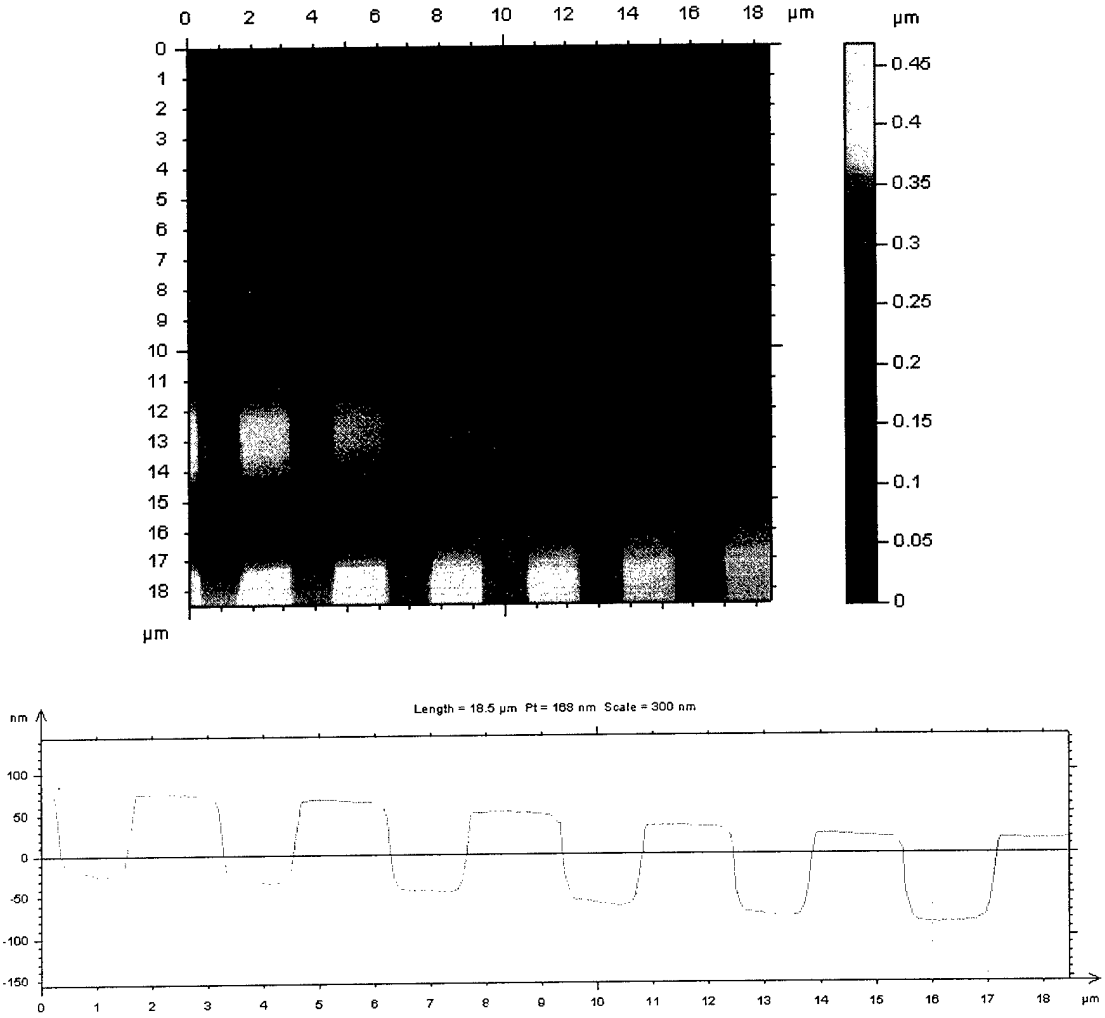

Figure 36: (a) 100°C AFM scan and (b) line profile of calibration grating showing both a minor temperature variation and an alignment skew

With the AFM scan module reaching a maximum temperature of 49.2°C during thermal cycling to 100°C, it is quite possible that the current design is capable of accurate testing at higher temperatures since the max safe operating temperature of the VISTA-

100 AFM is 100°C [Ref. 43]. However, due to possible permanent damage to the TGZ02 calibration grating, further elevated temperature testing was not conducted at this time.

C. REMARKS AND RECOMMENDATIONS

With the controlled atmosphere chamber and hot-stage combined with the VISTA-100 AFM, accurate *in-situ* thermal cycling experiments of thin metallic films is possible to temperatures of at least 100°C. Although this temperature is lower than that experienced by thin metallic films during fabrication, the mapping of at least a portion of the deformation history of thin metallic films subjected to thermal cycling is achievable.

There are several improvements to the controlled-atmosphere chamber and hot-stage which will aid in increasing experimental temperatures and accuracy. First, a smaller higher density heater will not only concentrate the heat input on the sample itself, but it will significantly reduce the amount of heat transfer by convection and radiation to the AFM scan module. This will not only enable the AFM to operate at a safe temperature, but it will help decrease instabilities such as laser drift during thermal cycling. Second, although costly, the use of ceramic-to-metal high vacuum rated electrical feedthroughs will enable the controlled atmosphere chamber to hold vacuum. The current design allows for the simple addition of ceramic-to-metal feedthroughs and a diffusion pump which would enable operating vacuum pressures of approximately 1×10^{-5} to 1×10^{-7} torr. This would not only eliminate the possibility of oxidation, but also limit the amount of heat convection from the heated surface to the AFM scan module. Third, increasing the insulation of the AFM scan module components and increasing the control of the cooling design will also increase both testing temperature

and measurement accuracy. And finally, switching from the standard Nanosensors Pointprobe® with a reflex coating to a probe without a reflex coating may decrease the effects from relatively small temperature changes. This can be accomplished by Thermal Centravision Inc. using the selected probe and a standard VISTA-100 cantilever tab.

These and other improvements can be easily incorporated into the current controlled-atmosphere with hot-stage design, eventually allowing for detailed *in-situ* studies of plastic deformation and interfacial sliding of thin metallic films on Si substrates during thermal cycling at elevated temperatures. This will enable a detailed mechanistic understanding of the interaction between the temperature-dependent stress state of the film and the resultant ineleastic deformation within the film and at the interface, leading to further understanding and improvements in microelectronic device fabrication, reliability, and performance.

VII. SUMMARY

1. The need for detailed *in-situ* studies of the plastic deformation of thin metallic films on Si substrates is shown by the *post-situ* results of thermally cycled Cu thin films on a Si substrate. Using an atomic force microscope (AFM), the Cu thin films were observed to *shrink* after successive thermal cycles. Thus, based on experimental data, it appears that due to the mismatch in the coefficients of thermal expansion and the net compressive stress history during the thermal cycling, Cu lines can experience the phenomenon of diffusionally-controlled interfacial sliding. Based on these *post-situ* results, the development of an experimental assembly to enable *in-situ* thermal cycling experiments is deemed essential to increase the understanding of film deformation and the reliability of microelectronic devices.
2. A controlled atmosphere chamber and hot-stage are incorporated into the design of the VISTA-100 AFM. The apparatus is able to provide a protective sample environment and conduct accurate AFM scans up to temperatures of at least 100°C. With this apparatus, accurate *in-situ* thermal cycling experiments to 100°C of thin metallic films are achievable, enabling a portion of the deformation history of thin metallic films to be studied.
3. It is recommended that several basic modifications to the apparatus be completed enabling accurate AFM scans through the range of microelectronic device fabrication temperatures for future *in-situ* thermal cycling experiments of thin metallic films.

THIS PAGE INTENTIONALLY LEFT BLANK

LIST OF REFERENCES

1. W.D. Nix, *Metallurgical Transactions A*, **20A**, 1989, pp. 2217-2245.

2. F.R. Brotzen, *International Materials Review*, **39**, 1994, pp. 24-45.

3. O. Kraft and W.D. Nix, *Journal of Applied Physics*, **83**, 1998, pp. 3035-3038.

4. W.D. Nix, *Scripta Materialia*, **39**, 1998, pp. 545-554.

5. J. Gupta, J.M.E. Harper, and M.D. Thouless, *Journal of Materials Research*, **8**, 1993, pp. 1845-1852.

6. M.D. Thouless, *Annual Review of Materials Science*, **25**, 1995, pp. 69-96.

7. Y.L. Shen and S. Suresh, *Journal of Materials Research*, **10**, 1995, pp. 1200-1215.

8. P.A. Flinn, D.S. Gardner, and W.D. Nix, *IEEE Transactions on Electron Devices*, **34**, 1987, pp. 689-698.

9. M.W. Chen and I. Dutta, *Applied Physics Letters*, **77**, 2000, pp. 4298-4300.

10. I. Dutta, M.W. Chen, K. Peterson, and T. Shultz, *Journal of Electronic Materials*, 2001, in press.

11. R. Nagarajan, I. Dutta, J.V. Funn, and M. Esmele, *Materials Science & Engineering A*, **259**, 1999, pp. 237-252.

12. I. Dutta, *Acta Materialia*, **48**, 2000, pp. 1055-1074.

13. J.V. Funn and I. Dutta, *Acta Metallurgica*, **47**, 1999, pp. 149-164.

14. P.A. Flinn, *Journal of Materials Research*, **6**, 1991, pp. 1498-1501.

15. R.J. Gleixner and W.D. Nix, *Journal of Applied Physics*, **86**, 1999, pp. 1932-1944.

16. A.I. Sauter, and W.D. Nix, *IEEE Transactions on Components, Hybrids and Manufacturing Technology*, **15**, 1992, pp. 594-600.

17. J. Gupta, J.M.E. Harper, J.L. Mauer IV, P.G. Blauner, and D.A. Smith, *Applied Physics Letters*, **61**, 1992, pp. 663-665.

18. Y.L. Shen, S. Suresh, and I.A. Blech, *Journal of Applied Physics*, **80**, 1996, pp. 1388-1398.

19. S.A. Campbell. *The Science and Engineering of Microelectronic Fabrication.* Oxford University Press, 1996.

20. W.S. Ruska. *Microelectronic Processing.* McGraw Hill, 1987.

21. K. Roll and H. Hoffman, *Review of Scientific Instruments*, **47**, 1976, pp. 1183-1185.

22. M. Murakami, *Acta Metallurgica*, **26**, 1978, pp. 175-183.

23. G. Cornella, S. Lee, W.D. Nix, J.C. Bravman, *Applied Physics Letters*, **83**, 1998, pp. 3035-3038.

24. A. Segmuller, J. Angilelo, and S.J. LaPlaca, *Journal Applied Physics*, **51**, 1980, pp. 6224-6230.

25. S.S. Berry, *Advances X-Ray Analysis*, **26**, 1983, pp. 255-258.

26. D.S. Gardner and P.A. Flinn, *IEEE Transactions on Electron Devices*, **35**, 1988, pp. 2160-2169.

27. Y.L. Shen and S. Suresh, *Acta Materialia*, **44**, 1996, pp. 1337-1348.

28. Y.L. Shen and S. Suresh, *Acta Materialia*, **43**, 1995, pp. 3915-3926.

29. A. Gouldstone, Y.L. Shen, S. Suresh, and C.V. Thompson, *Journal of Materials Research*, **13**, 1998, pp. 1956-1966.

30. D.V. Zhmurkin, T.S. Gross, L.P. Buchwalter, *Journal of Electronic Materials*, **26**, 1997, pp. 791-797.

31. R.N. Castellano. *Semiconductor Device Processing.* Gordon and Breach Science Publishers, 1993.

32. Burleigh Instruments Inc., VISTA Scanning Probe Microscope Operating Manual, 1998.

33. C.W. Smith and C.M. Smith, *The Scientist*, **15**, 2001, pp. 23-28.

34. Kinetic Systems Inc., Kinetic Systems Product Manual, www.kineticsystems.com, 2001.

35. R. Raj and M.F. Ashby, *Metallurgical Transactions*, **2**, 1971, p. 1113.

36. K.K. Chawla. *Composite Materials: Science and Engineering*. Springer, New York, 1987.

37. Nanosensors Corp., Pointprobe^{R} Product Manual, www.nanosensors.com, 2001.

38. Jack Roberts, Thermal Centravision Inc., Sales Engineer, private communication, 2001.

39. L.M. Gignac, K.P. Rodbell, C. Cabral Jr., P.C. Andricacos, P.M. Rice, R.B. Beyers, P.S. Locke, and S.J. Klepeis, *Proceedings of Materials Research Society Symposium*, **564**, 1999, p. 373.

40. MDC Vacuum Products Corporation, Volume 10 Product Manual, 1999.

41. Hawke Cable Glands LTD, Hawke Transit System Product Manual, 2001.

42. L.S. Darken and R.W. Gurry. *Physical Chemistry of Metals*. McGraw-Hill, 1953.

43. Jim Zobel, Burleigh Instruments Inc., VISTA-100 Managing Engineer, private communication, 2001.

44. G. Binning, C.F. Quate, and Ch. Gerber, *Physics Review Letters*, **56**, 1986, pp. 930-933.

THIS PAGE INTENTIONALLY LEFT BLANK

INITIAL DISTRIBUTION LIST

1. Defense Technical Information Center 2
   8725 John J. Kingman Rd., STE 0944
   Ft. Belvoir, Virginia 22060-6218

2. Dudley Knox Library 2
   Naval Postgraduate School
   411 Dyer Rd.
   Monterey, California 93943-5101

3. Naval Engineering, Code 34 1
   Naval Postgraduate School
   Monterey, California 93943-5100

4. Department Chairman, Code ME/Mc 1
   Department of Mechanical Engineering
   Naval Postgraduate School
   Monterey, California 93943-5000

5. Professor Indranath Dutta, Code ME/Du 1
   Department of Mechanical Engineering
   Naval Postgraduate School
   Monterey, California 93943-5000

6. Dr. Bruce A. MacDonald 1
   Program Director
   Metal, Ceramics, and Electronic Materials
   National Science Foundation
   Materials Research Division
   4201 Wilson Blvd. Rm. 1065
   Arlington, Virginia 22230

7. Lieutenant Thomas E. Shultz, USN 2
   1288 Cresthill Road
   El Cajon, CA 92021